REPORT DOCUMENTATION PAGE

AFRL-SR-AR-TR-04-

0557

1. REPORT DATE (DD-MM-YYYY)	2. REPORT TYPE	3. DATES COVERED (From - To)
15-10-2004	Final	11-July-2002 - 30-June-2004

4. TITLE AND SUBTITLE
High Order Electromagnetic Modeling for High Frequency

5a. CONTRACT NUMBER
F49620-02-C-0038

5b. GRANT NUMBER

5c. PROGRAM ELEMENT NUMBER
62702E

6. AUTHOR(S)
Moore, John T.

5d. PROJECT NUMBER

5e. TASK NUMBER

5f. WORK UNIT NUMBER

7. PERFORMING ORGANIZATION NAME(S) AND ADDRESS(ES)
Science Applications International Corporation
1901 South First Street, Suite D-1
Champaign, IL 61820-7449

8. PERFORMING ORGANIZATION REPORT NUMBER

9. SPONSORING/MONITORING AGENCY NAME(S) AND ADDRESS(ES)
Air Force Office of Scientific Research (AFOSR)/NM
4015 Wilson Blvd /Mail Room 713
Arlington, VA 22203

10. SPONSOR/MONITOR'S ACRONYM(S)
AFOSR/NM

11. SPONSOR/MONITOR'S REPORT NUMBER(S)

12. DISTRIBUTION/AVAILABILITY STATEMENT
Distribution Statement A. Approved for public release; distribution is unlimited.

13. SUPPLEMENTARY NOTES

20041109 010

14. ABSTRACT
The goals of this project were to insert mature physical theory of diffraction (PTD) based phenomenology models into the Xpatch® computational electromagnetics (CEM) prediction codes and analysis tools. Several incremental length diffraction coefficient derivations were identified as candidates for inclusion. The shadow boundary incremental length diffraction coefficient (ILDC) capability was integrated based on the significant correction it applies to the physical optics current discontinuity in the neighborhood of the shadow region of smooth scatterers. The truncated wedge incremental length diffraction coefficient was implemented because it provides fully polarimetric responses for a large range of edge discontinuities and surface areas, and it avoids discontinuities and singularities associated with earlier wedge ILDC derivations. A detailed study of creeping waves was performed to supplement the shadow boundary ILDC development. All functionality developed under this project underwent comprehensive unit, integration, and regression level testing prior to delivery.

15. SUBJECT TERMS
Xpatch®, computational electromagnetics, ILDC, and creeping wave

16. SECURITY CLASSIFICATION OF:			17. LIMITATION OF ABSTRACT	18. NUMBER OF PAGES	19a. NAME OF RESPONSIBLE PERSON
a. REPORT	b. ABSTRACT	c. THIS PAGE			Dr. Arje Nachman
U	U	U	SAR	55	19b. TELEPHONE NUMBER (Include area code) (703)-696-8427

Contract No: F49620-02-C-0038

High Order Electromagnetic Modeling for High Frequency

Final Report

For the Period: 11 July 2002 – 30 June 2004

Unclassified

Submitted by:
SAIC-DEMACO
1901 S First Street, Suite D-1
Champaign, IL 61820-7449

Prepared for:
Air Force Research Laboratory (AFRL)
Air Force Office of Scientific Research (AFOSR)/NM
801 North Randolph Street
Arlington, VA 22203

Final Report: September 2004

1. **Contract:** Air Force Research Lab # F49620-02-C-0038
2. **Title:** High Order Electromagnetic Modeling for High Frequency
3. **Duration:** July 11, 2002 – June 30, 2004
4. **Report Period:** July 11, 2002 – June 30, 2004
5. **Reported By:** John Moore, Program Manager and Principal Investigator
6. **Report Date:** October 15, 2004

TABLE OF CONTENTS

I. INTRODUCTION

The goals of this project are to insert mature diffractive scattering and radiation technology into the Xpatch® computational electromagnetics (CEM) prediction codes and analysis tools. Diffraction plays a significant role in the radar scattering from targets consisting of smooth surfaces or joints, and numerous applications such as Reduced Radar Cross Section (RRCS) aircraft design, threat signature exploitation, automatic target recognition (ATR), and sensor fusion (SF) research and development can benefit from the accuracy improvements associated with diffractive scattering models. The diffraction enhancements developed under this project shall be delivered to the Air Force customer as well as offered in general Xpatch® releases to the United States Department of Defense (DoD) scattering and radiation community at large for multiple wideband applications.

During Year 1 (the fourteen months from July 2002 through August 2003) the contractor integrated a robust implementation of the newly developed Air Force Office of Scientific Research (AFOSR) mathematical formulations for higher-order scattering mechanisms into Xpatch® to calculate more accurate current estimates in the lit as well as the shadow region of the targets. Specifically, the contractor reformulated truncated wedge incremental length diffraction coefficients (ILDCs) and shadow boundary ILDCs and inserted them into Xpatch®. In addition, the supporting Xpatch® geometry tools were modified to support these new ILDC capabilities. The contractor employed appropriate testing, validation criteria, and documentation to enable the rapid transition of this software technology to a broad range of United States DoD applications.

During Year 2 (the nine months from September 2003 to June 2004) the contractor performed a detailed study of creeping waves to supplement the shadow boundary ILDC development of Year 1. This study was motivated by the role of creeping waves as a source of interaction between installed antenna arrays and air frames. A prototypical creeping wave ray tracer was utilized for the purposes of the study. Future efforts beyond the scope of this project will focus on development of a robust creeping wave ray tracer.

II. SHADOW BOUNDARY ILDC DEVELOPMENT

A. Introduction

The contractor has implemented the shadow boundary ILDCs in both their simple and extended form into Xpatch®. The reformulation of the detailed expressions of the new shadow-boundary ILDCs for Xpatch® has been the primary task under this effort with close collaboration with Dr. Arthur Yaghjian. The underlying implementation of the ILDCs in Xpatch® was designed such that the geometric representation of the underlying curvature and shadow boundary of the target initial graphics exchange specifications (IGES) CAD file are used to calculate all the necessary information for the ILDCs, without requiring intervention by the Xpatch® user.

Without the added capabilities realized with shadow boundary ILDCs, Xpatch® forward scattering degrades for smooth structures. Figure 1 compares the bistatic scattering from a circular cylinder computed by Xpatch® without shadow boundary ILDCs to the exact solution. The Xpatch® solution degrades as the observation angle moves from the lit to the shadow zone.

To illustrate the importance of the shadow boundary ILDC capability, consider the imaging problem illustrated in Fig. 2 of a tank shadowed by a hill's crest. Currently SAR simulations are line-of-sight based. Generic scene modeling will miss the tank based on the first-order assumption that no incident energy reaches the tank. However the true radar will see returns from the tank. The application of shadow boundary ILDCs along the ridge crest permits Xpatch® modeling of these types of scenarios.

B. Technical Overview

Shadow boundary incremental length diffraction coefficients (SB-ILDCs) are not a complete solution to capturing the physics embodied in the diffraction and radiation of energy in the shallow shadow region. However, SB-ILDCs do represent a significant improvement over the standard physical optics (PO) formulation by providing a far-field correction to the discontinuous PO fields along the shadow boundary (which abruptly step from finite on the lit side to zero on the shadowed side). In effect the shadow boundary ILDCs soften the shadow and improve the bistatic scattering prediction of Xpatch®, but they remain inadequate for deep shadow region modeling of creeping waves traveling long distances along geodesic paths.

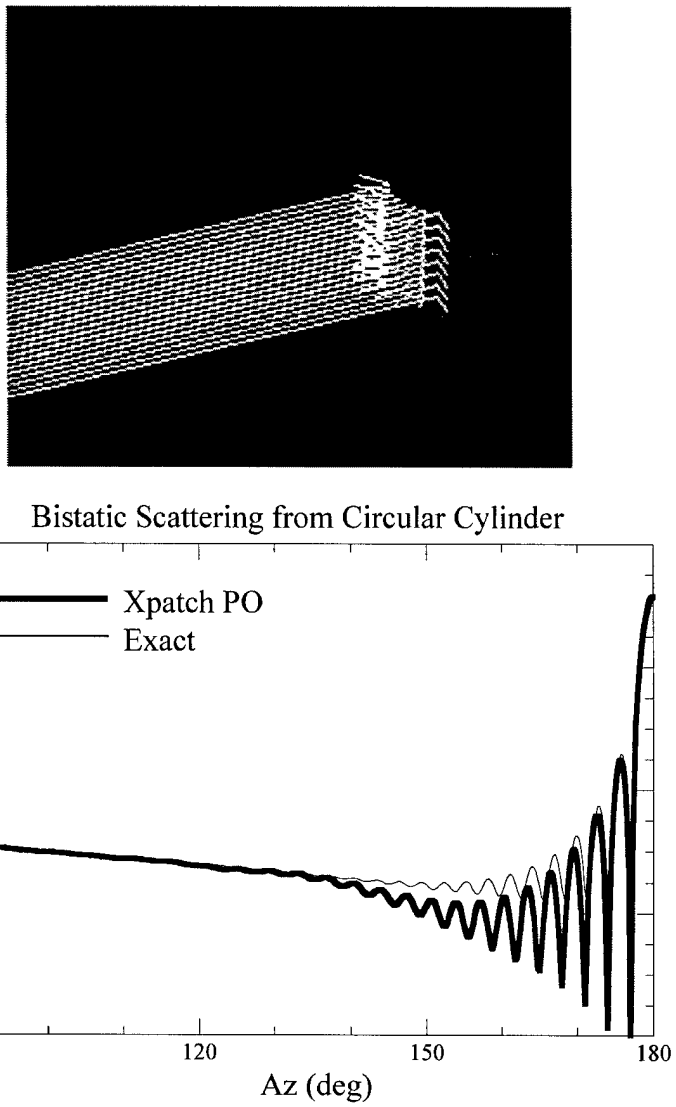

Fig. 1. A 6" radius cylinder (top) of 2" height. Bistatic scattering comparison of Xpatch® with an exact modal solution (bottom). $El_{inc}=El_{obs}=0^{o}$, $Az^{inc}=0^{o}$, 18.8 GHz, TM_z polarization. $ka = 60$.

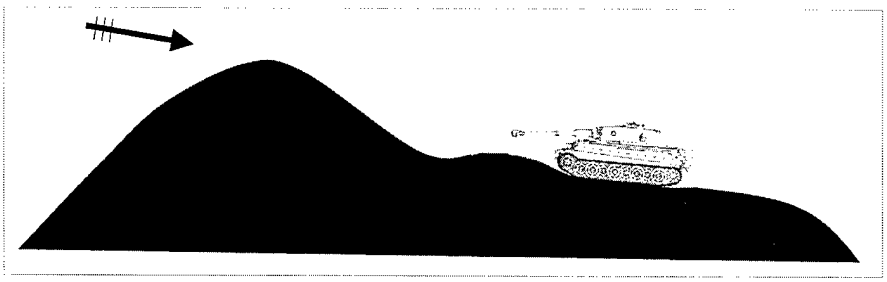

Fig. 2. Tank shadowed by the crest of a hill. A geometrical optics or physical optics approach will assume that no incident energy reaches the target when in fact radar energy is diffracted by the shadow boundary formed at the crest of the hill and illuminates the target.

The present formulation is based upon the ILDC work. [1]. The approach is built on closed-form 2-D expressions of scattering from the circular cylinder [2] and the previous ILDC work on the prolate spheroid [3]. Non-uniform (NU) currents in the vicinity of the shadow boundary are the difference between the exact currents and those predicted by PO. These currents are significant in the immediate vicinity of the shadow boundary. The shadow boundary ILDC currents are the NU currents on a circular cylinder that locally conforms to the surface of the scatterer.

The geometric parameters needed to calculate the shadow boundary ILDCs are the shadow boundary curve, the vector normal to the shadow boundary surface and the scatterer's radius of curvature across the shadow boundary. This short list of parameters can be efficiently computed, providing a low computational cost to using the shadow boundary ILDCs.

The equations for the shadow boundary ILDCs are given below. The integral of $d\vec{E}^{SB}$ along the shadow boundary estimates the electric field due to the NU currents.

$$d\vec{E}^{SB}(\theta_{0l},r_l,\theta_l,\phi_l) = E_{0l}^{TM}\, d\vec{E}_{TM}(\theta_{0l},r_l,\theta_l,\phi_l) + E_{0l}^{TE}\, d\vec{E}_{TE}(\theta_{0l},r_l,\theta_l,\phi_l) \tag{1}$$

where

$$\begin{aligned} dE_{TM}(\theta_{ol},r_l,\theta_l,\phi_l) = -|kdz_l|\frac{e^{ikr_l}}{kr_l}\frac{e^{-i\pi/4}}{\sqrt{8\pi}}\Big\{\Big[e^{ika_c\sin\alpha}F_z^{SB}(ka_c,-\alpha) + \\ + e^{-ika_c\sin\alpha}F_z^{SB}(ka_c,-\alpha)\Big]_{k\to k\sin\theta_{0l}} \\ \cdot\frac{\sin\theta_1}{\sin\theta_{0l}}\hat{\theta}_l + \Big[e^{ika_c\sin\alpha}F_z^{SB}(ka_c,-\alpha) \\ - e^{ika_c\sin\alpha}F_z^{SB}(ka_c,-\alpha)\Big]_{k\to k\sin\theta_{0l}} \\ \frac{1}{\sin\alpha}\Big[\sin\phi_l\hat{\theta}_l + \Im(\theta_{ol},\theta_l,\phi_l,t)\hat{\phi}_l\Big]\Big\} \end{aligned} \tag{2}$$

$$\begin{aligned} dE_{TE}(\theta_{ol},r_l,\theta_l,\phi_l) = |kdz_l|\frac{e^{ikr_l}}{kr_l}\frac{e^{-i\pi/4}}{\sqrt{8\pi}}\Big\{\Big[e^{ika_c\sin\alpha}G_z^{SB}(ka_c,-\alpha) + \\ + e^{-ika_c\sin\alpha}G_z^{SB}(ka_c,-\alpha)\Big]_{k\to k\sin\theta_{0l}} \\ \cdot\frac{\sin\theta_1}{\sin\theta_{0l}}\hat{\phi}_l + \Big[e^{ika_c\sin\alpha}G_z^{SB}(ka_c,-\alpha) \\ - e^{-ika_c\sin\alpha}G_z^{SB}(ka_c,-\alpha)\Big]_{k\to k\sin\theta_{0l}} \\ \frac{1}{\sin\alpha}\Big[\sin\phi_l\hat{\phi}_l + \Im(\theta_{ol},\theta_l,\phi_l,t)\hat{\theta}_l\Big] \\ -\sqrt{\frac{2}{\pi}}e^{i\pi/4}\cot\theta_{0l}\sin\theta_l\hat{\theta}_l\Big\} \end{aligned} \tag{3}$$

with

$$\Im(\theta_{ol},\theta_l,\phi_l,t)=\cos\phi_l\cos\theta_l+t\cot\theta_{0l}\sin\theta_l \tag{4}$$

$$t=\left[\frac{\sin\theta_l\cos\phi_l-\cot\theta_{0l}(\cos\theta_{0l}+\cos\theta_l)}{\sin\theta_{0l}}\right] \tag{5}$$

$$\alpha=\cos^{-1}t \tag{6}$$

$$\begin{aligned}F_z^{SB}(ka_c,,\psi)=-\Bigg\{&\left[\frac{1.255}{\sqrt{2\pi}}\left(\frac{ka_c}{2}\right)^{1/3}e^{i\pi/12}\exp\left[-\pi\left(\frac{ka_c}{2}\right)^{1/3}|\psi|\right]\right.\\&\left.+\frac{e^{i\pi/4}\exp\left[-(ka_c/32)|\psi|^3\right]}{2\sqrt{2\pi}\tan|\psi/2|}\right]\\&\cdot\exp\left(-i2ka_c\sin\left|\frac{\psi}{2}\right|\right)\\&+\left[\sqrt{\frac{ka_c|\psi|}{16}}\exp\left[-(ka_c)^{1/3}|\psi|\right]\exp\left[i\frac{\pi}{4}e^{-2ka_c|\psi|^2}\right]\right.\\&\cdot\left(1-e^{-2ka_c|\psi|}\right)-\frac{i\exp\left[-(ka_c/2)^{2/3}|\psi|^2\right]}{2\sqrt{2\pi}\sin|\psi/2|}\\&\left.\exp\left[-i\left(ka_c\sin|\psi|+\frac{\pi}{4}\right)\right]\right]\Bigg\},\qquad 0\le\psi\le\pi\end{aligned} \tag{7}$$

$$
\begin{aligned}
F_z^{SB}(ka_c,\psi) = -\Bigg\{ & \Bigg[\sqrt{\frac{ka_c|\psi|}{16}} \exp\left[-(ka_c)^{1/3}|\psi|\right] \\
& \cdot \exp\left[-i\frac{\pi}{4}e^{-2ka_c|\psi|^2}\right]\left(1-e^{-2ka_c|\psi|}\right) \\
& + \frac{i\exp\left[-(ka_c/2)^{2/3}\right]\psi|^2}{2\sqrt{2\pi}\sin|\psi/2|}\Bigg] \\
& \exp\left[i\left(ka_c\sin|\psi|\right)-\frac{\pi}{4}\right] + \sqrt{\frac{\pi}{2}}\left(\frac{ka_c}{2}\right)^{1/3} \\
& \exp\left[i\left(ka_c|\psi|+\frac{\pi}{12}\right)\right] \\
& \left[\frac{0.038}{\pi}\sec h\left(\frac{(ka_c)^{2/3}|\psi|^2}{\pi}\right)\right. \\
& \left. - \sum_{s=1}^{S_{\max}} \frac{\exp\left[i\alpha_s(ka_c/2)^{1/3}e^{i\pi/3}|\psi|\right]}{\sqrt{\alpha_s}}\right], \quad -\pi \le \psi \le 0
\end{aligned}
\tag{8}
$$

$$
\begin{aligned}
G_z^{SB}(ka_c,\psi) = -\Bigg\{ & \Bigg[\frac{1.089}{\sqrt{2\pi}}\left(\frac{ka_c}{2}\right)^{1/3} e^{i\pi/12}\exp\left[-\pi\left(\frac{ka_c}{2}\right)^{1/3}|\psi|\right] \\
& + \frac{e^{i\pi/4}\exp\left[-(ka_c/32)|\psi|^3\right]}{2\sqrt{2\pi}\tan|\psi/2|}\Bigg] \\
& \cdot \exp\left(-i2ka_c\sin\left|\frac{\psi}{2}\right|\right) \\
& + \left[\sqrt{\frac{ka_c|\psi|}{16}}\exp\left[-(ka_c)^{1/3}|\psi|\right]\exp\left[i\frac{\pi}{4}e^{-2ka_c|\psi|^2}\right]\right. \\
& \left. \cdot\left(1-e^{-2ka_c|\psi|}\right) - \frac{1-1/2\exp\left[-(ka_c/2)^{2/3}|\psi|^2\right]}{i\sqrt{2\pi}\tan|\psi/2|}\right. \\
& \left. \exp\left[-i\left(ka_c\sin|\psi|+\frac{\pi}{4}\right)\right]\right\}, \qquad 0 \le \psi \le \pi
\end{aligned}
\tag{9}
$$

$$
\begin{aligned}
G_z^{SB}(ka_c,\psi) = -\Bigg\{ & \Bigg[\sqrt{\frac{ka_c|\psi|}{16}} \exp\left[-(ka_c)^{1/3}|\psi|\right] \\
& \cdot \exp\left[-i\frac{\pi}{4}e^{-2ka_c|\psi|^2}\right]\left(1-e^{-2ka_c|\psi|}\right) \\
& + \frac{1-1/2\exp\left[-(ka_c/2)^{2/3}\right]|\psi|^2}{i\sqrt{2\pi}\tan|\psi/2|} \Bigg] \\
& \exp\left[i(ka_c\sin|\psi|)-\frac{\pi}{4}\right] + \sqrt{\frac{\pi}{2}}\left(\frac{ka_c}{2}\right)^{1/3} \\
& \exp\left[i\left(ka_c|\psi|+\frac{\pi}{12}\right)\right] \\
& \left[\frac{0.469}{\pi}\sec h\left(\frac{(ka_c)^{2/3}|\psi|^2}{\pi}\right)\right. \\
& \left. - \sum_{s=1}^{S_{\max}} \frac{\exp\left[i\beta_s(ka_c/2)^{1/3}e^{i\pi/3}|\psi|\right]}{\sqrt{\beta_s}}\right], \quad -\pi \le \psi \le 0
\end{aligned}
\tag{10}
$$

$$
\begin{aligned}
\alpha_s &= \left[3\pi(4s-1)/8\right]^{2/3} \\
\beta_s &= \left[3\pi(4s-1)/8\right]^{2/3}
\end{aligned}
\tag{11}
$$

$$
S_{\max} = Int\left[10/\left((ka_c)^{1/2}|\psi|^{3/2}\right)+1\right] \tag{12}
$$

The above expressions assume a harmonic dependence of $e^{-i\omega t}$ (trivial transformations need to be made when comparisons to Xpatch® are made because Xpatch® assumes a $e^{j\omega t}$ time-dependence). The wave propagation constant in free-space is given by $k = \omega/c$, where c is the speed of light and $\omega > 0$. The subscript l denotes a local coordinate system (x_l, y_l, z_l) whose origin is a point P_{SB} on the shadow boundary. The positive y_l-axis is in the direction of the external normal $\hat{n}_{SB}$ to the surface of the scatterer at P_{SB}. The z_l-axis is the tangent to the shadow boundary curve at P_{SB}, with a positive direction assigned to the z_l-axis by requiring that $\hat{k}^{inc} \cdot \hat{x}_l = \hat{k}^{inc} \cdot (\hat{n}_{SB} \times \hat{z}_l) > 0$. The spherical polar angle θ_{0l} is the angle between $-\hat{k}^{inc}$ and $\hat{z}_l$.

The angles θ_l and ϕ_l are the spherical angles of the direction to the observation point; $\hat{\theta}_l$ and $\hat{\phi}_l$ are the corresponding unit spherical angle vectors; r_l is the distance from P_{SB} to the observation point, and dz_l is the differential length along the shadow boundary at P_{SB}. The scalar a_c is the radius of the perfectly electric conducting (PEC) circular cylinder whose axis is parallel to the shadow boundary. The functions $F_z^{SB}(ka_c,\psi)$ and $G_z^{SB}(ka_c,\psi)$ are the 2-D electric and magnetic far-fields radiated by the non-uniform currents at the top shadow boundary of the cylinder

illuminated by a TM and TE plane wave, respectively, of unit amplitude normally incident in the positive x-direction. The coefficients E_{0l}^{TM} and E_{0l}^{TE} are the complex amplitudes of the TM and TE components of the incident field at P_{SB}, that is

$$\vec{E}^{inc}(P_{SB}) = -E_{0l}^{TM}\hat{\theta}_{0l} + E_{0l}^{TE}\hat{y}_l \tag{13}$$

where E_{0l}^{TM} and E_{0l}^{TE} are given by

$$\begin{aligned} E_{0l}^{TM} &= -Z_o \hat{n}_{SB} \cdot \vec{H}^{inc}(P_{SB}) \\ &= \left(\hat{k}^{inc} \times \hat{n}_{SB}\right) \cdot \vec{E}^{inc}(P_{SB}) \end{aligned} \tag{14}$$

and

$$E_{0l}^{TE} = \hat{n}_{SB} \cdot \vec{E}^{inc}(P_{SB}) \tag{15}$$

and $\hat{\theta}_{0l} = \hat{n}_{SB} \times \hat{k}^{inc}$ and $\hat{y}_l = \hat{n}_{SB}$. The summations over the creeping waves indexed by s, which continue to infinity, have been truncated to $S_{\max}$. This implies that creeping waves are not followed or modeled deep within the shadowed region. The circular cylinder coordinates centered on this cylinder are denoted by (ρ, ψ) (see Fig. 3).

Results presented in the next section of the report demonstrate the effectiveness of this formulation. In summary, the main assumptions made in deriving these formulas are as follows:

1) Plane-wave incident field
2) Constant radius of curvature in the longitudinal direction at the shadow boundary
3) Infinite radius of curvature in the transverse direction at the shadow boundary
4) Creeping wave truncation
5) Phase correction added based on empirical data

C. Shadow Boundary Search Algorithm

The shadow boundary search algorithm calculation effort is of *O(n)*, which is similar to PO. It requires exhaustive interrogation of the surface geometry and must be recalculated for every new direction of incident illumination. The calculation is performed for curved surfaces only. The algorithm first breaks the surfaces into sufficiently small (typically 0.1 λ) patches. The shadow boundary search algorithm then computes the quantity $\hat{n} \cdot \bar{k}_{inc} = 0$ at the four corners of the patch.

Figure 4 shows a surface patch, with its corners labeled with a blue dot. Finally, the algorithm interpolates zero-crossings to estimate the shadow contour. This procedure locates the shadow boundary contour, where $\hat{n} \cdot \bar{k}_{inc} = 0$. A sophisticated root finder is not necessary for this calculation, and the piecewise linear search approach converges towards the true shadow boundary contour as the discretization size is made finer.

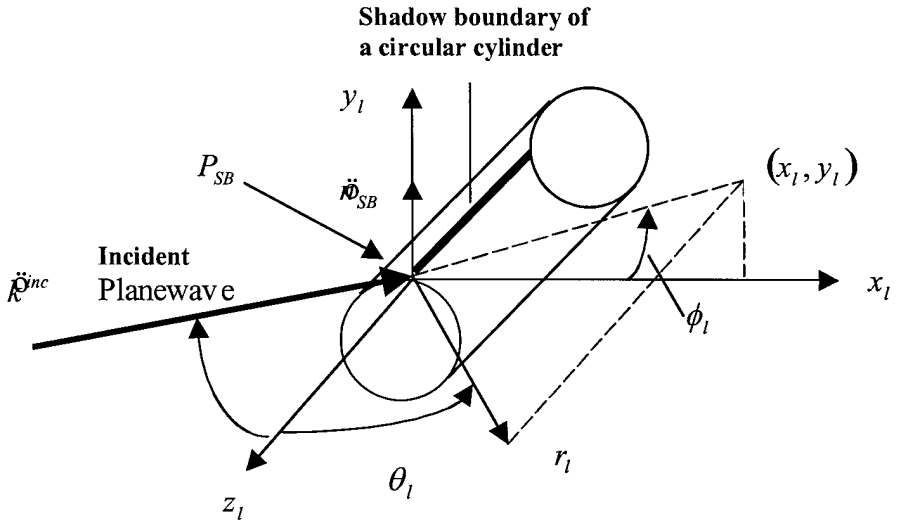

Fig. 3. Shadow boundary quantities relating to the illumination of a circular cylinder. The local coordinate system is defined such that the axis of the cylinder is in the z-direction.

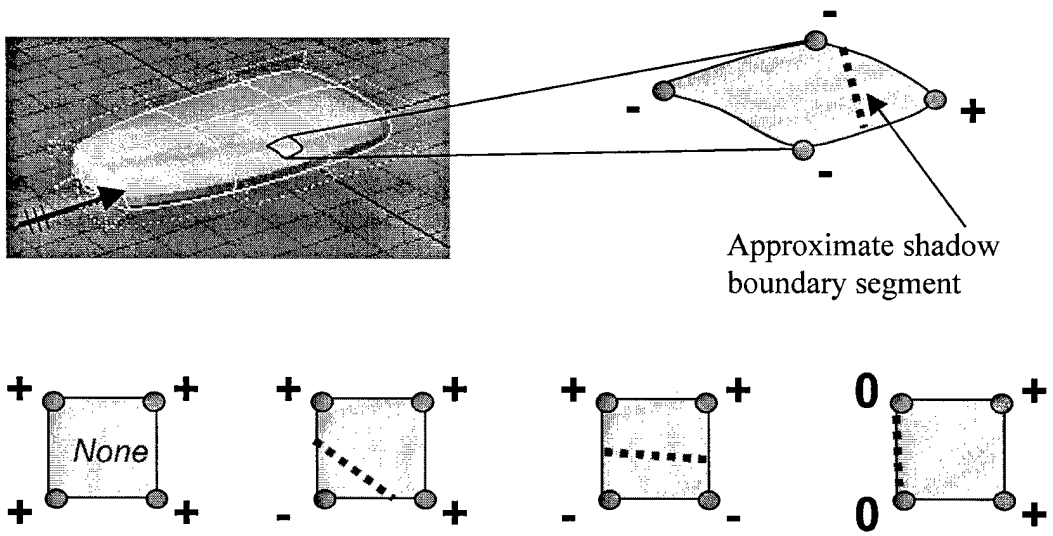

Fig. 4. Illustration of the potential illumination scenarios affecting a small cell of a curved patch. The shadow boundary is approximated by a line segment within each affected cell.

D. Results and Discussion

This section presents computational results illustrating the efficacy of the shadow boundary ILDCs. The first result is the bistatic (VV-pol) scattering from a circular cylinder illuminated perpendicular to its axis. The boundary search algorithm places two segments on the cylinder's shadow boundary as shown in Fig. 5. The results show that Xpatch® with the shadow boundary correction is a significant improvement over the PO solution and is nearly identical to the exact solution.

The second example is a six-inch radius sphere. Here, the shadow boundary is modeled by segments located along the equator of the sphere. Figure 6 identifies the segmented shadow

boundary on the sphere. The neighboring graph illustrates the accuracy gained by including the SB-ILDCs in the computation. The Xpatch® with SB-ILDC result is nearly identical to the exact solution while the Xpatch®-PO result exhibits significant deviations.

The next example investigates the SB-ILDC contribution to the scattering solution. The graphs shown in Fig. 7 compare the exact minus the PO solution to the SB-ILDC (only) calculated scattering. The agreement is good to about 45 dB down. The discrepancies can be traced to the 20 cells per wavelength PO approximation.

The SB-ILDC plus PO solution maintains good accuracy compared to the standard Xpatch® solution as the scatterer size decreases. Figure 8 illustrates the scattering from a sphere as its size decreases from $ka = 20$ to $ka = 6$. Figure 9 shows the scattering from an elliptical cylinder. This geometry has a non-constant radius of curvature, suggesting a more complex field variation along the shadow boundary. Figure 10 shows the scattering from a spheroid illuminated by a plane wave with at $Az = -45°$ incidence. Internally, Xpatch® employs Euler's formula to calculate the local radius of curvature along each subdivision of the shadow boundary contour.

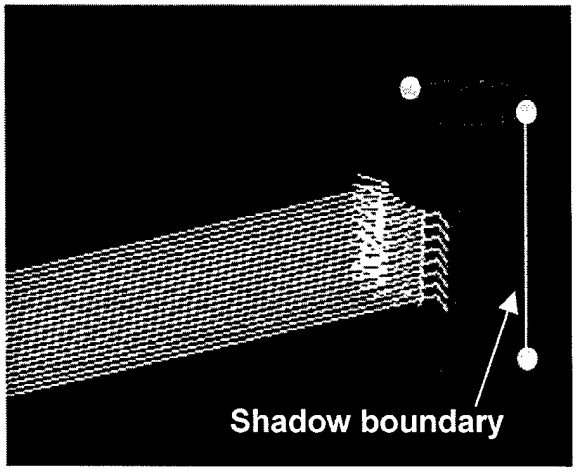

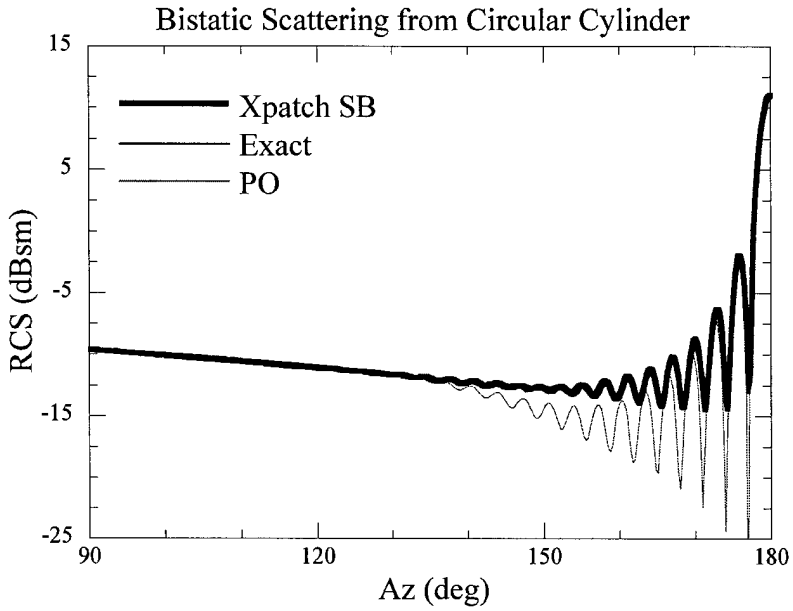

Fig. 5. The 6" radius cylinder (top) of Fig. 1 with the ILDC segments shown. Bistatic scattering comparison of Xpatch® with shadow boundary correction versus an exact modal solution (bottom). $El_{inc}=El_{obs}=0^o$, $Az^{inc}=0^o$, 18.8 GHz, TM_z polarization. $ka = 60$.

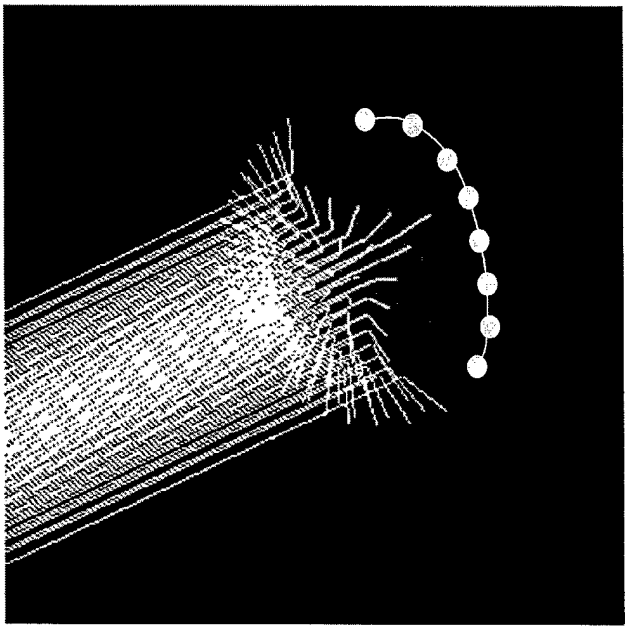

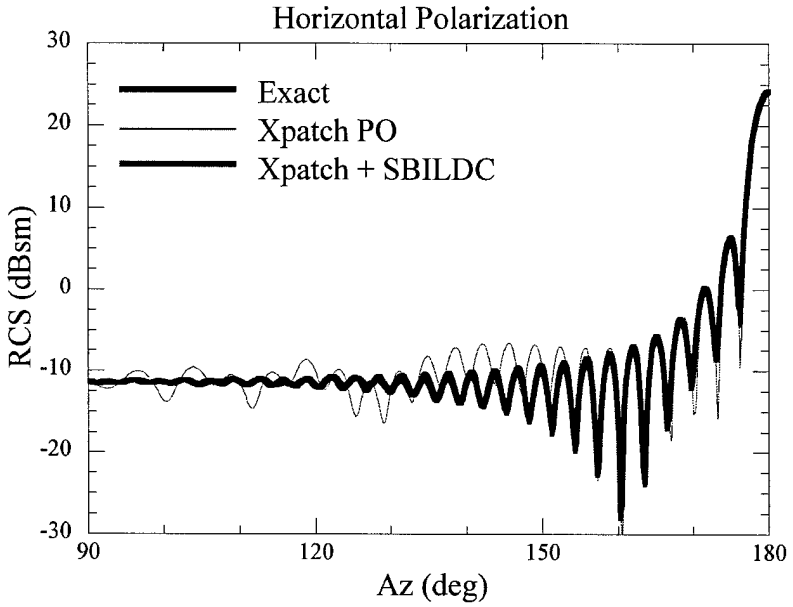

Fig. 6. A 6" radius sphere (top) with the shadow boundary segments shown. Bistatic scattering comparison of Xpatch® with shadow boundary correction versus an exact modal solution (bottom). $El_{inc}=El_{obs}=0^{o}$, $Az^{inc}=0^{o}$, 18.8 GHz, TM_z polarization. $ka = 60$.

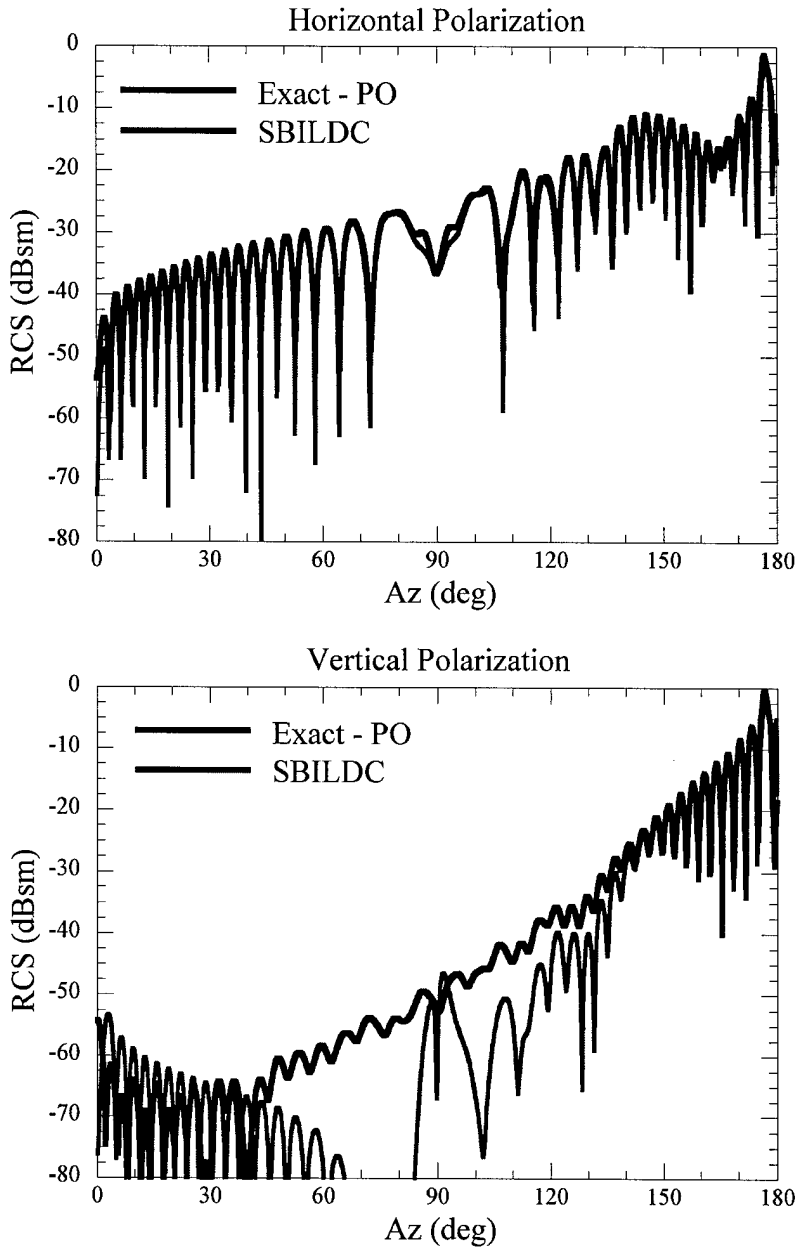

Fig. 7. The isolated shadow boundary ILDC contributions (physical optics component removed) for the sphere of Fig. 6.

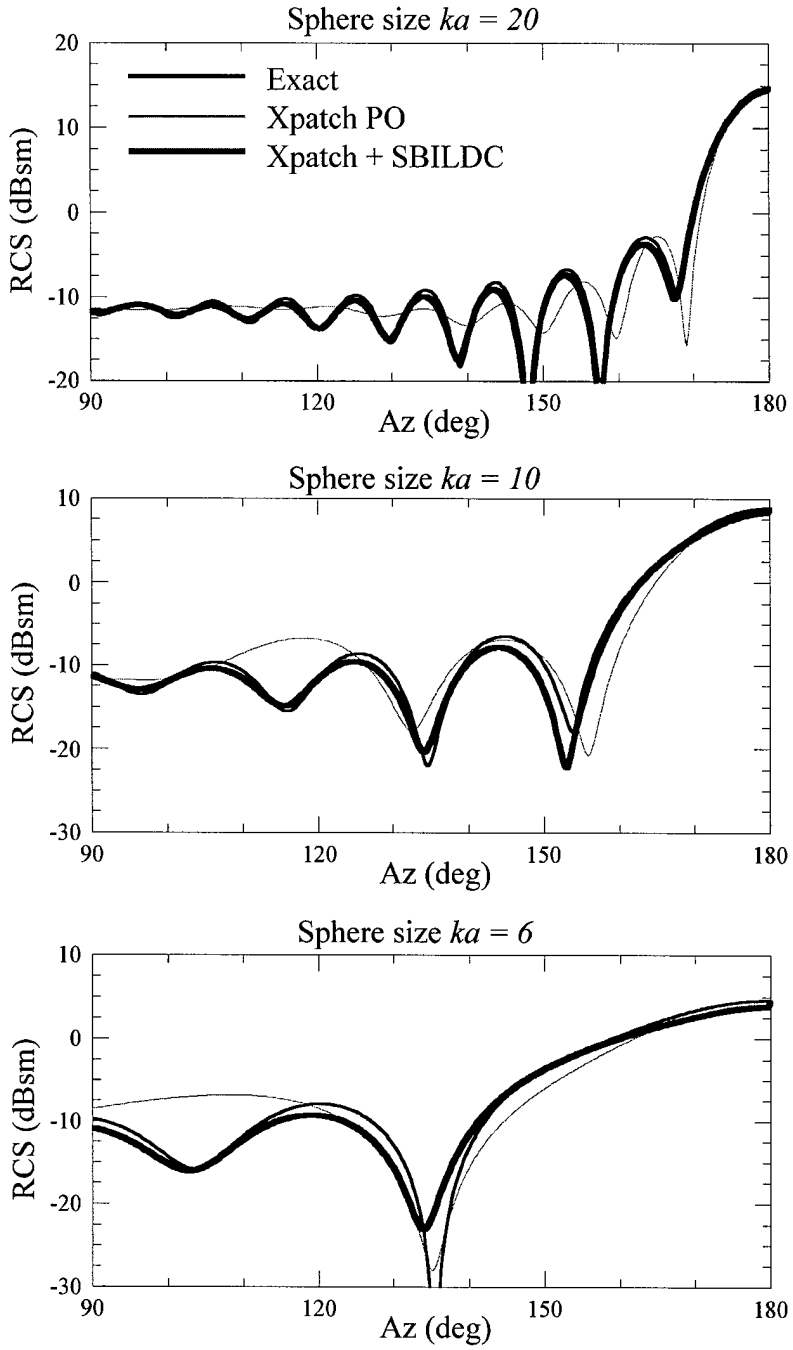

Fig. 8. Accuracy degradation of the shadow boundary ILDCs as a function of sphere size for HH-pol and bistatic observations.

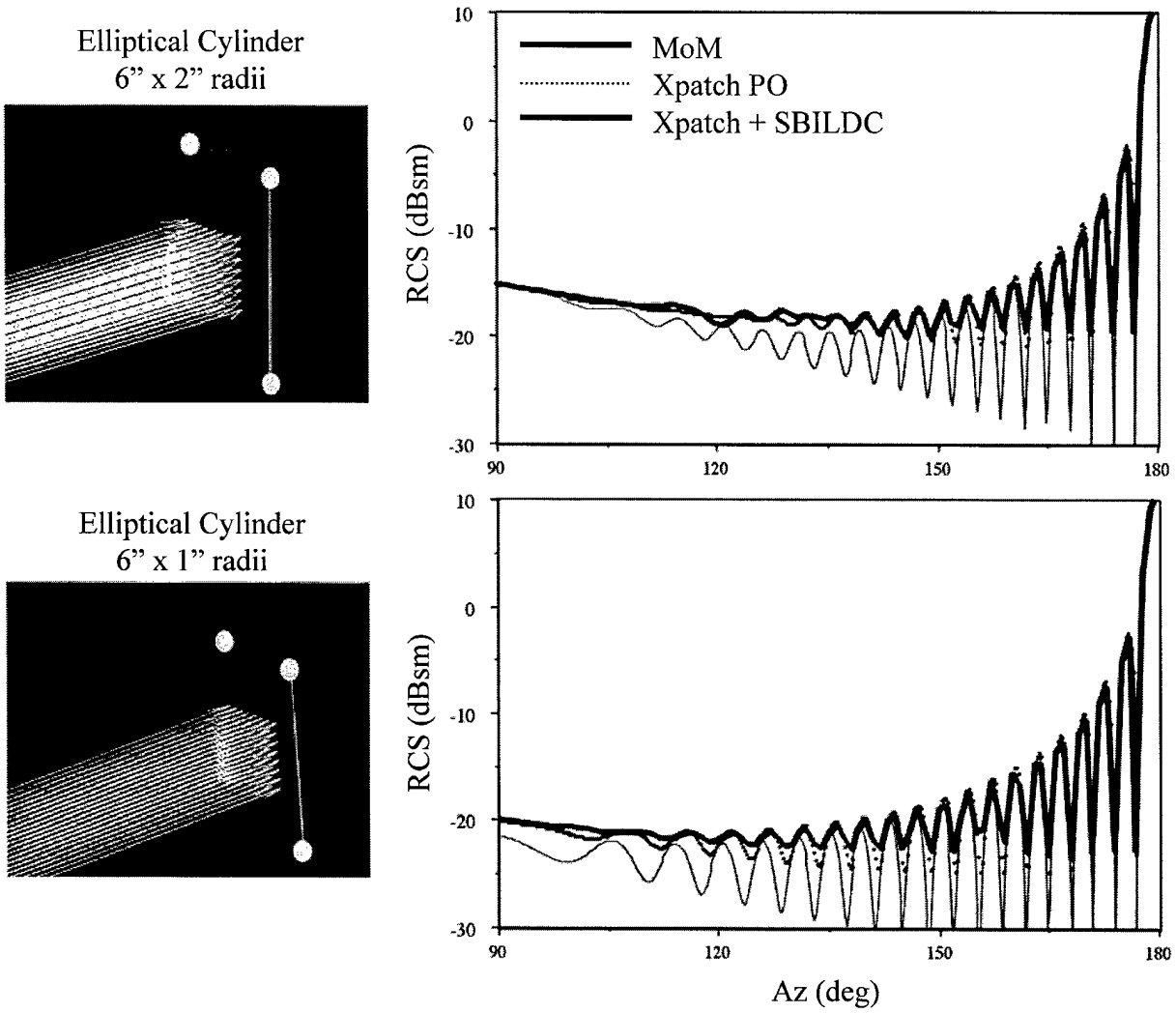

Fig. 9. Accuracy degradation of the shadow boundary ILDCs for non-constant radius of curvature, HH-pol and bistatic observations. Top ρ_{ildc} =*0.667"* and bottom ρ_{ildc} = *0.167"*.

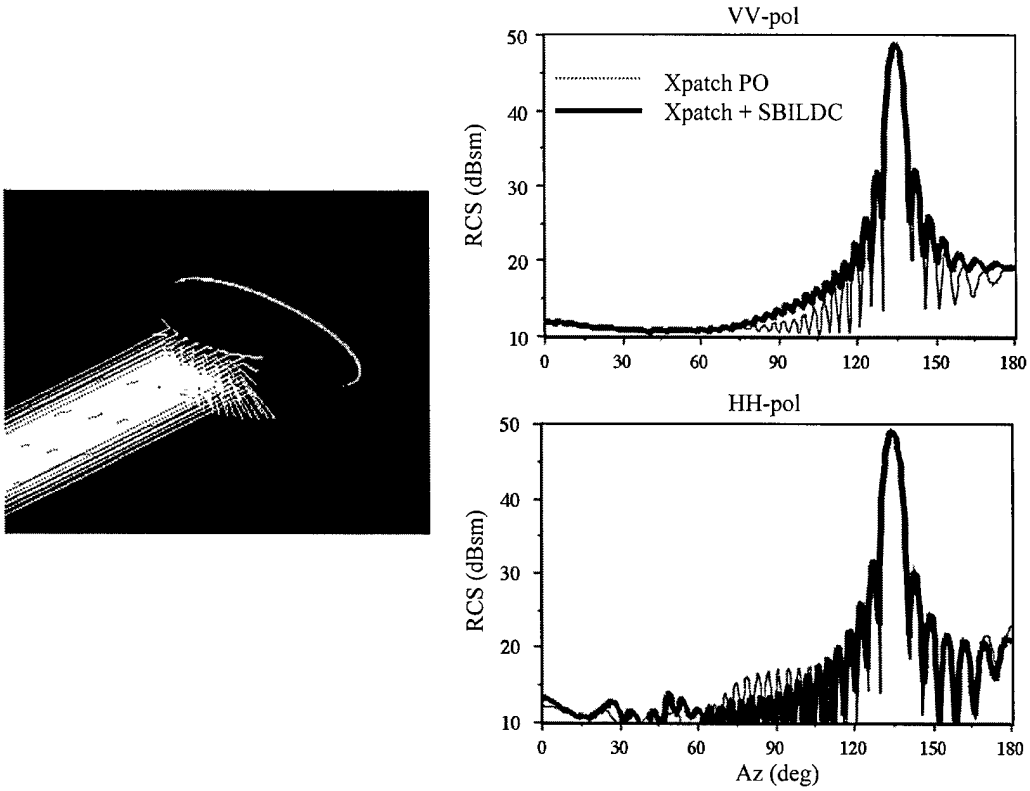

Fig. 10. Bistatic scattering from the prolate spheroid for $Az = -45^{o}$ incidence with $ka = 50$ and $kb = 25$. The shadow boundary determined by Xpatch® is shown in light green and agrees with the closed form solution [3] to the shadow boundary contour.

E. Summary

The implementation of shadow boundary ILDCs in Xpatch® has been demonstrated by the improvement of scattering predictions for large cylinders and spheres with a wide range of sizes. Scatterers with changing radii of curvature were successfully modeled, and adequate accuracy was realized even for rapidly changing radii of curvature. The implemented shadow boundary search algorithm was verified against trivially defined shadow boundaries for the cylinder and sphere, as well as for more complex shadow boundaries, such as the prolate spheroid at off-axis incidence angles.

III. TRUNCATED WEDGE ILDC DEVELOPMENT

A. Introduction

The contractor has reformulated the truncated wedge incremental length diffraction coefficients (TW-ILDCs) and has inserted them into both the time- and frequency-domain versions of Xpatch® in a manner that will facilitate their use for complex targets. User-friendly tools for the truncated wedge ILDCs, (*e.g.*, a tool to extract the "other" side of the wedge) as well as a robust and accurate electromagnetic (EM) implementation, have been implemented under this task. Validation and testing of the truncated wedge ILDCs have been accomplished with complex targets represented by curved surface IGES CAD formats.

The sole use of PO to calculate the scattering from various PEC bodies results in significant inaccuracies for bodies possessing edges. Inclusion of the fringe wave (FW) field, a field that represents diffraction effects due the edge, improves the accuracy of such calculations. The FW field is calculated from an integral along incremental strips located on a canonical wedge or half-plane [4-7]. The standard Xpatch® code calculates these wedge ILDCs. Symbolically the FW field is expressed as $E^{FW} = E^{GTD} - E^{PO}$ for the semi-infinite wedge. The fields are expressed as a semi-infinite integral along the projection of the Keller cone on the wedge face. This integral can be expressed as a line integral along a differential segment, and the resulting contribution is referred to interchangeably as an equivalent edge current (EEC) or incremental length diffraction coefficient (ILDC).

The use of truncated wedge ILDCs is motivated by the following problem (see Fig. 11). The classical wedge ILDCs formulated in [4-7] possess non-removable "Ufimtsev" singularities when ***kinc*** approaches grazing and ***kobs*** is near ***kinc***. The classical wedge ILDCs also exhibit discontinuities in the fringe wave field due to the use of non-physical semi-infinite current strips.

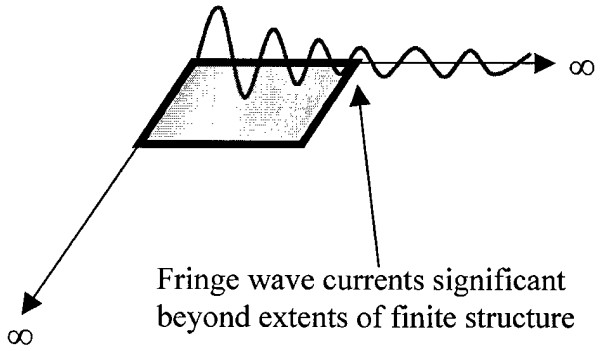

Fig. 11. Fringe wave currents emanating from the left edge of a four-sided patch. The fringe wave currents are strong for incident fields perpendicularly polarized relative to the edge while fringe wave currents due to parallel incidence are negligible.

B. Technical Overview

As stated above, the classical wedge ILDCs exhibit infinities. Figure 12 shows the scattering from an equilateral triangle with a two-meter side length and a one-meter cylinder height. The scatterer has nine diffracting edges. The yellow edge is nearly at grazing incidence, primarily along the skew direction. Surface currents in the direction of the Keller cone are non-decaying

[8]. A singularity exists due to a non-converging integral. ($k^{obs} \rightarrow 0$ or π in the edge local coordinate system.)

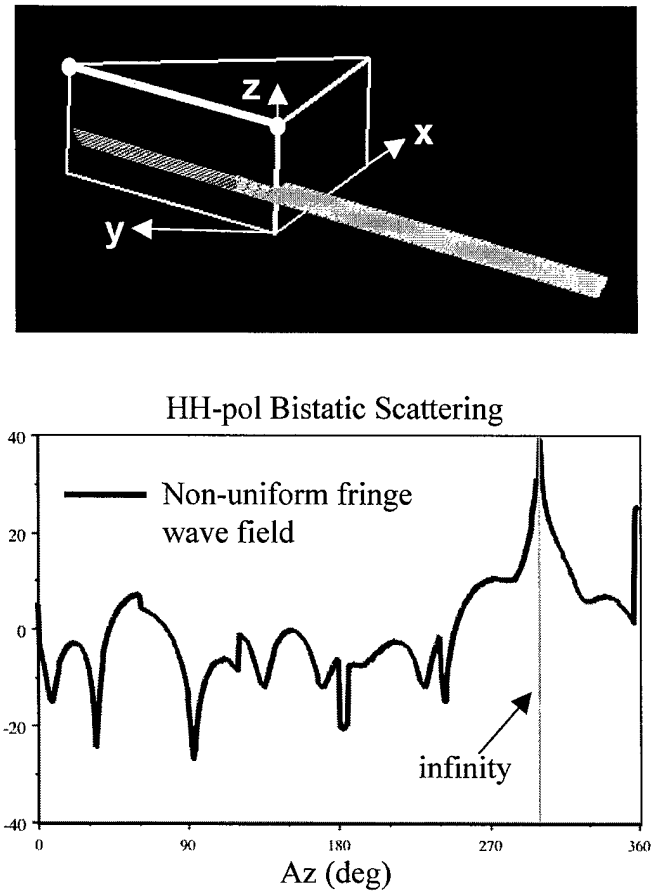

Fig. 12. Infinities and discontinuities in the radar cross-section (RCS) arising from the single orange wedge ILDC (top) as calculated using the classical ILDC formulation. The physical optics component of the scattered field is not included in order to emphasize the behavior due to wedge diffraction.

The wedge ILDC formulation implemented in Xpatch® differs from the rigorously derived wedge ILDCs in that the Keller-Ufimtsev physical theory of diffraction (PTD) coefficients with singular terms are omitted. While the infinities of Fig. 12 are avoided, this omission of terms results in numerous discontinuities in the computed RCS magnitude and phase. Figure 13 shows the discontinuities in the predicted RCS of a triangular cylinder.

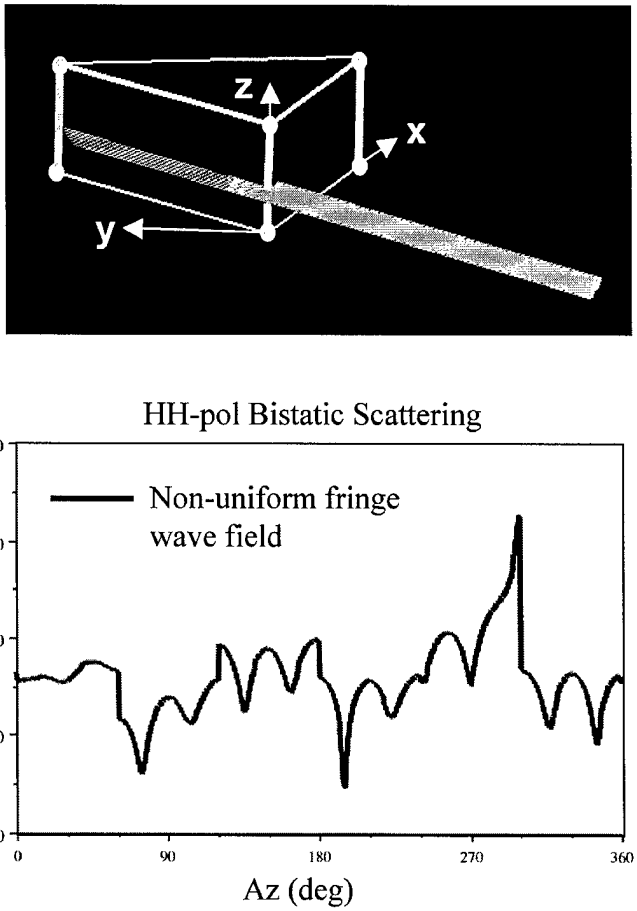

Fig. 13. Discontinuities in the RCS arising from the three orange wedge ILDCs (top) as calculated by Xpatch® using modified form of classical ILDC formulation. The physical optics component of the scattered field is not included in order to emphasize the behavior due to wedge diffraction.

C. The Truncated Wedge Algorithm

In order to improve upon the wedge ILDCs used in the standard Xpatch® code, truncated wedge ILDCs are employed. Developed by Johansen [8], these TW-ILDCs are well-behaved for all directions of incidence and observation and yield a finite value when the strip length goes to zero.

The implementation of the TW-ILDCs is a follows. First each edge is associated with its adjoining faces. As shown in Fig. 14, face one has four edges; face two has three edges; face three has four edges, and so forth. Then, differential strips are traced along each face, and integrations of the fringe wave contributions along the finite length strips are calculated. These finite integrations are guaranteed to converge. The fringe wave current, $J^{FW} = J^{UTD} - J^{PO}$ is restricted to L and accounts for the transition region (small electrical distances from the edge) and remains valid for large L extending well beyond the transition region.

The face association criteria are: shared end points, at least one shared normal, and formation of a closed polygon. The criteria are calculated automatically by Xpatch®, and users can intervene

via the ModelMan® CAD tool if special cases such as interior edges (not modeled by TW-ILDCs) form part of a wedge face.

The effort required to calculate the TW-ILDCs compared to classical wedge ILDCs is increased due to presence of Fresnel integrals. Also, the truncated segments vary with incidence angle and position, requiring new calculations for each angle of incidence and sample point along the edge, as displayed in Fig. 15.

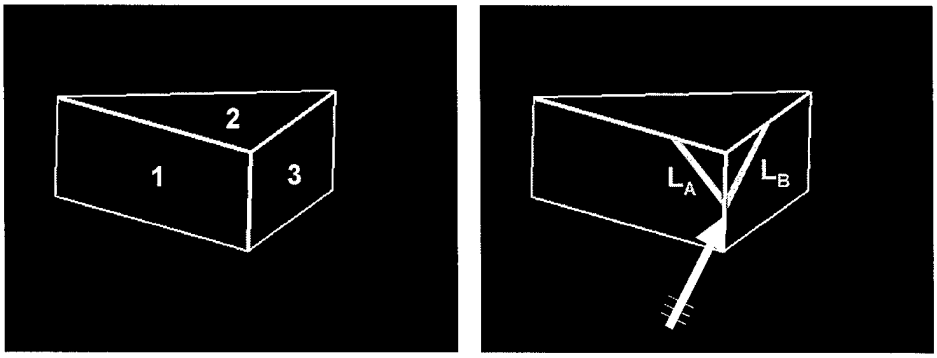

Fig. 14. Face and edge associations for the triangular wedge of Fig. 12. Edges which touch (or nearly touch to within an acceptable tolerance) and possess matching normals on at least one of their sides are considered to be associated. Shown on the right in orange are the two fringe wave path segments emanating from a hit point on the center edge and traveling until they reach an associated edge.

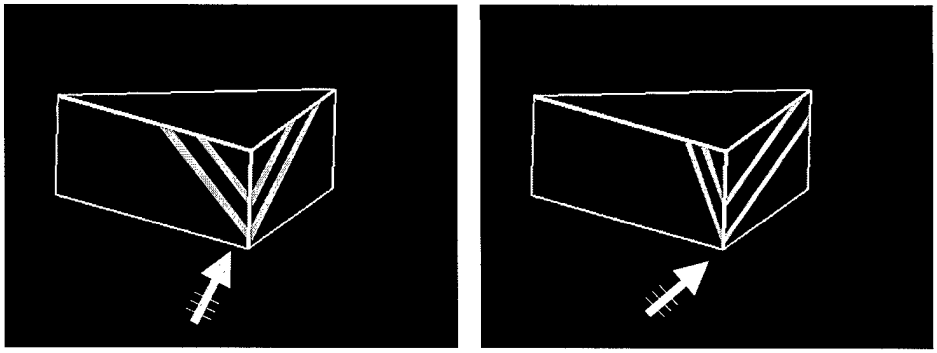

Fig. 15. Illustration of how varying angles of incidence result in different current strip path directions and path lengths. Truncated wedge current strips are a function of hit point, incidence angle, arrangement of neighboring associated edges, as well as frequency and wedge angle.

D. Results and Discussion

To illustrate the efficacy of the new TW-ILDCs the scattering from a triangular cylinder has been calculated. For this example the incident angle is normal to the edges (see Fig. 16), with three edges illuminated. A comparison is made between the old ILDC method, the truncated wedge ILDC method, and the 2-D moment method solution with PO subtracted out. Note that the truncated wedge solution is continuous across the aspect of illumination. The non-physical infinities associated with the old wedge ILDCs have been eliminated.

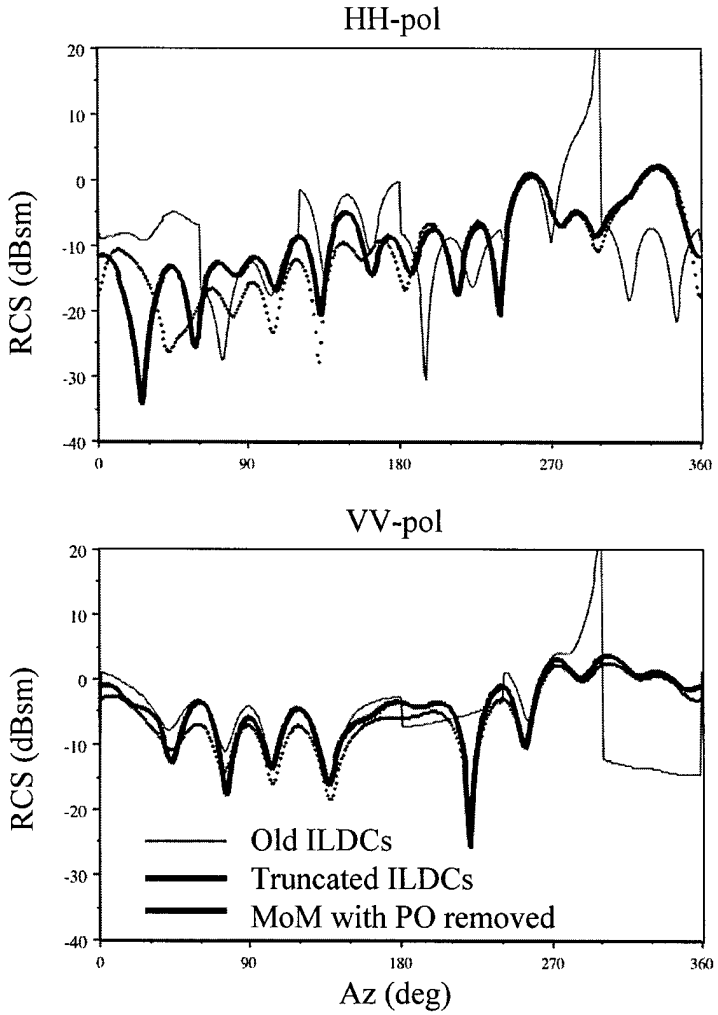

Fig. 16. Comparison of the new truncated wedge ILDCs for the wedge configuration of Fig. 12. The physical optics component of the scattered field is not included in order to emphasize the behavior due to wedge diffraction.

Figure 17 illustrates the old ILDC and new TW-ILDC scattering from a plate at skew incidence. This example is a square PEC plate with a side length of 0.5 meters (3 λ), illuminated at a frequency of 1.799 GHz. It has four knife edges connected to two faces. The incident direction angles are elevation, 45 degrees and azimuth, -45 degrees. The observation azimuth angle is fixed at 45 degrees, with the elevation ranging from 0 to 180 degrees.

A final example is the "pencil" geometry of Fig. 18. This case was originally developed at the University of Illinois during studies of the Fast Illinois Solver Code (FISC) in June 2003. A circular cylinder 3 m in length and 0.1 m radius is capped at one end with a circular plate, and the other end terminates in a circular cone of length 0.167 m. The frequency of interest is 3 GHz, and the incident vector is directly broadside to the cylinder (perpendicular to the axis of the cylinder).

The pencil of Fig. 18 possesses a shadow boundary which exists along the cylinder and the cone. The principal scattering due to shadow boundary diffraction is expected to arise from the cylinder

because the shadow boundary along the cone is only a few tenths of a wavelength in length and is represented by segments corresponding to diminishing radii of curvature. A single truncated wedge face is placed along the flat circular cap at the other end of the pencil geometry. Shown in Fig. 19 is a comparison of the physical optics and full wave results for the bistatic scattering from the pencil geometry. When the truncated wedge contributions are included, the agreement with the full wave solution is much improved (see Fig. 20). Finally, when the shadow boundary ILDC contributions are included in addition to the truncated wedge contributions, further agreement is achieved (see Fig. 21). The improvements due to the shadow boundary ILDCs will be strongest in the forward scattering direction. Shown in Fig. 22 is a magnified view of the main lobe of the pencil scattering in which the shadow boundary contribution is necessary to correct the magnitude of the scattering by approximately 1 dB. Neither physical optics alone nor physical optics with the truncated wedge contributions are capable of correctly predicting the forward scattering from the pencil geometry.

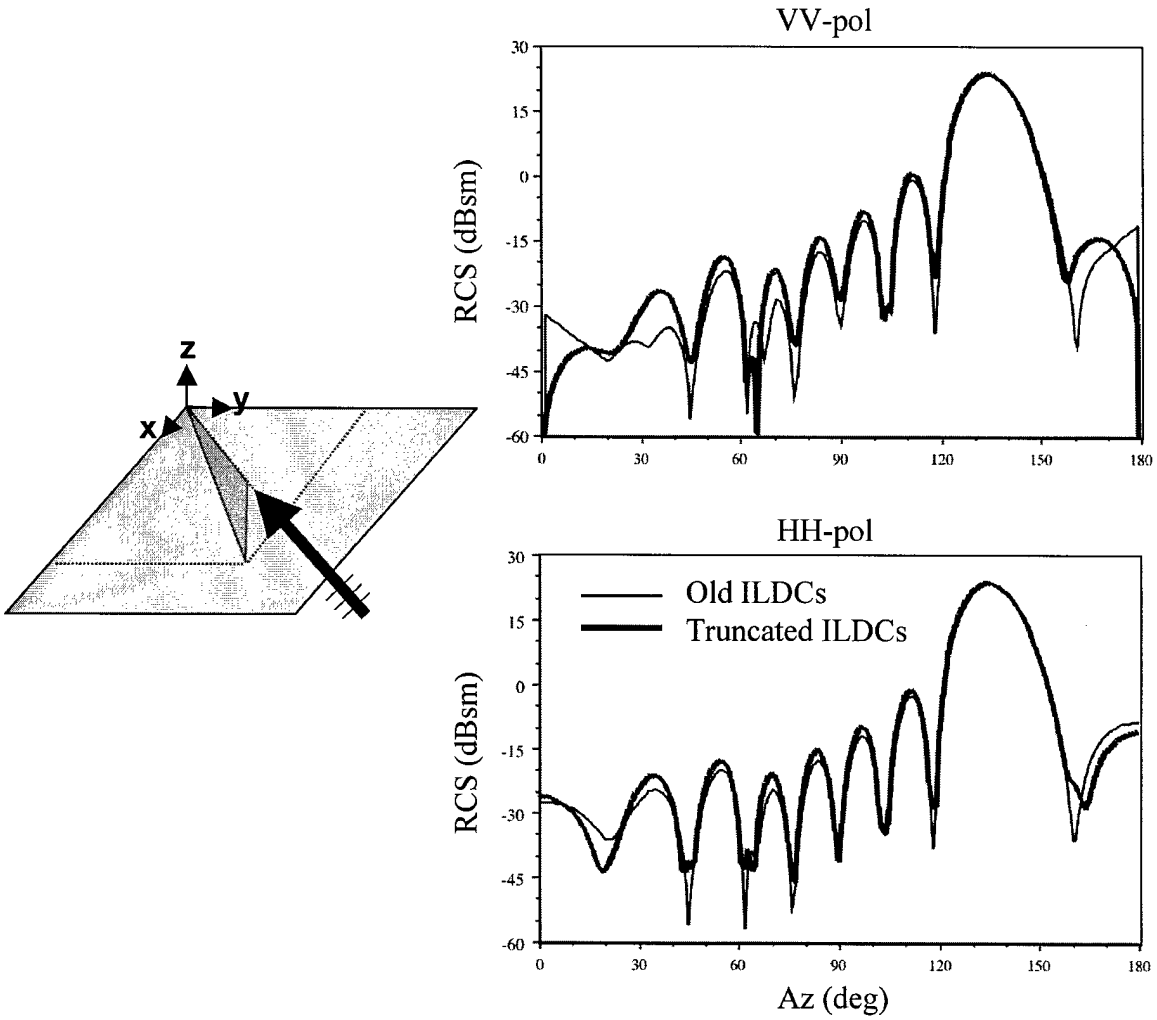

Fig. 17. A square plate 0.5 m on a side. Bistatic scattering comparison of Xpatch® between old and new ILDCs. $El_{inc}=El_{obs}=45^{o}$, $Az^{inc}=-45^{o}$, 1.799 GHz.

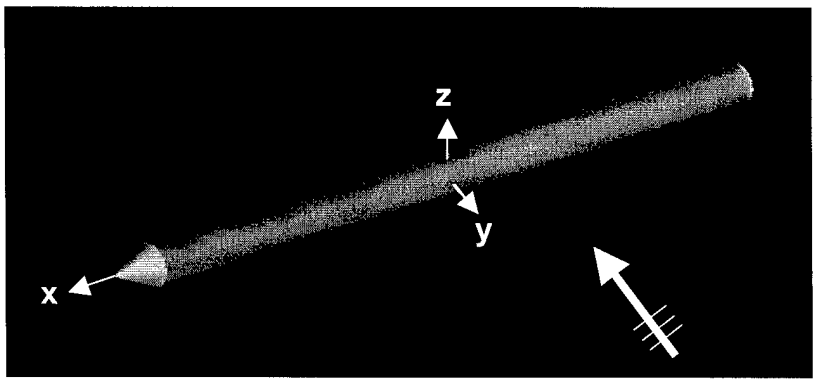

Fig. 18. The pencil geometry composed of a cone and cylinder and flat circular end cap (hidden).

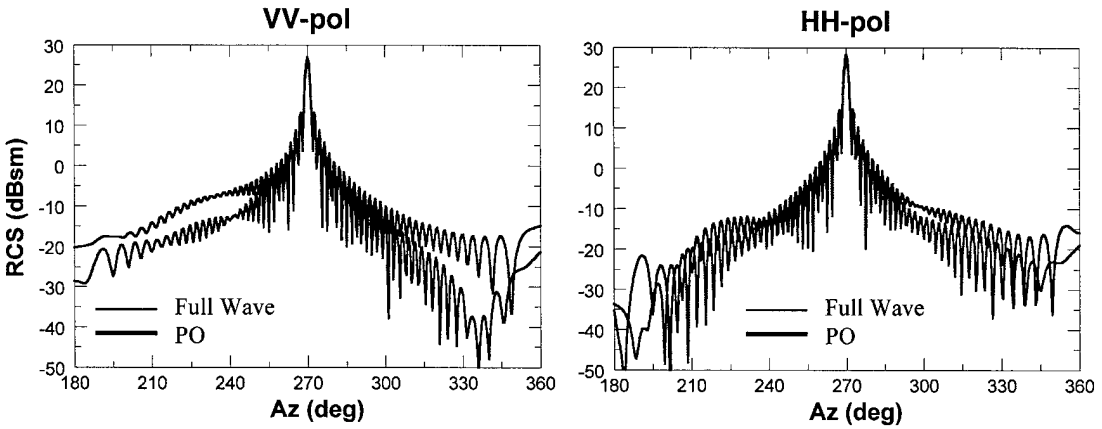

Fig. 19. Bistatic scattering from the pencil: Full wave vs. physical optics.

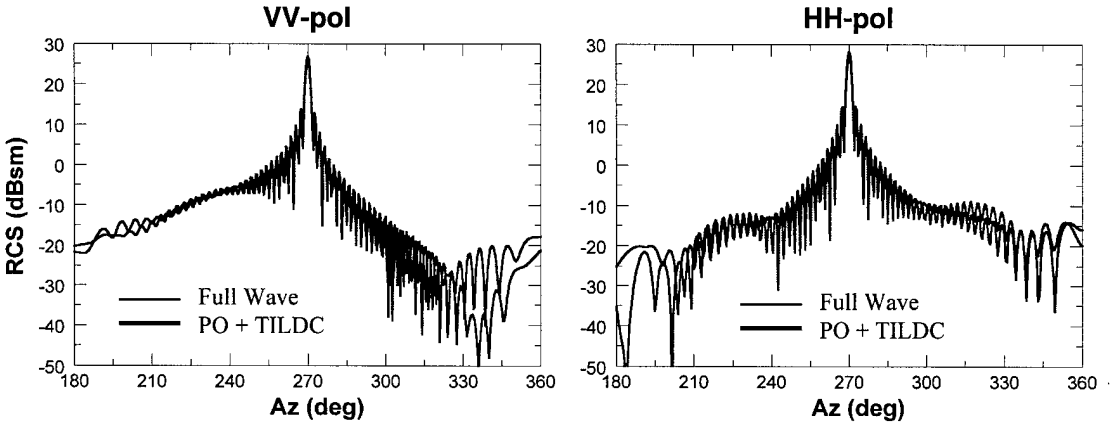

Fig. 20. Bistatic scattering from the pencil with truncated wedge contributions included.

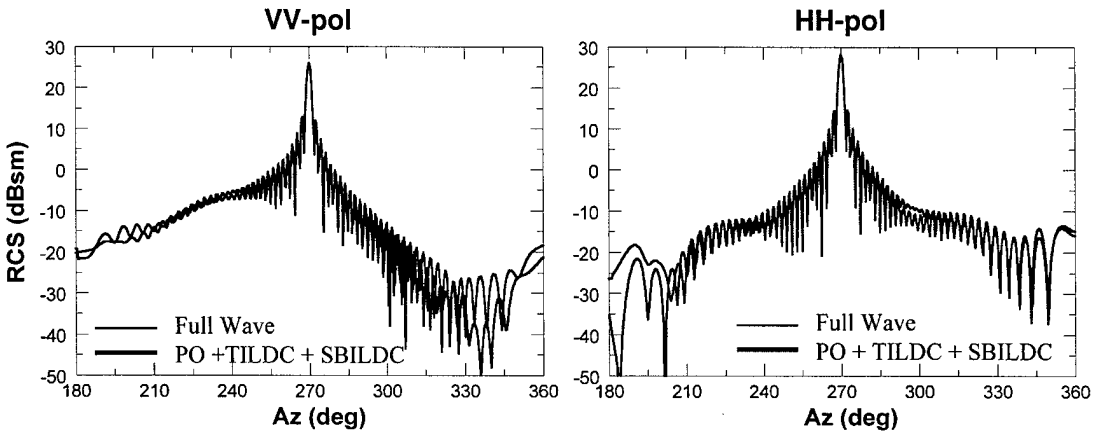

Fig. 21. Bistatic scattering from the pencil with shadow boundary and truncated wedge contributions included.

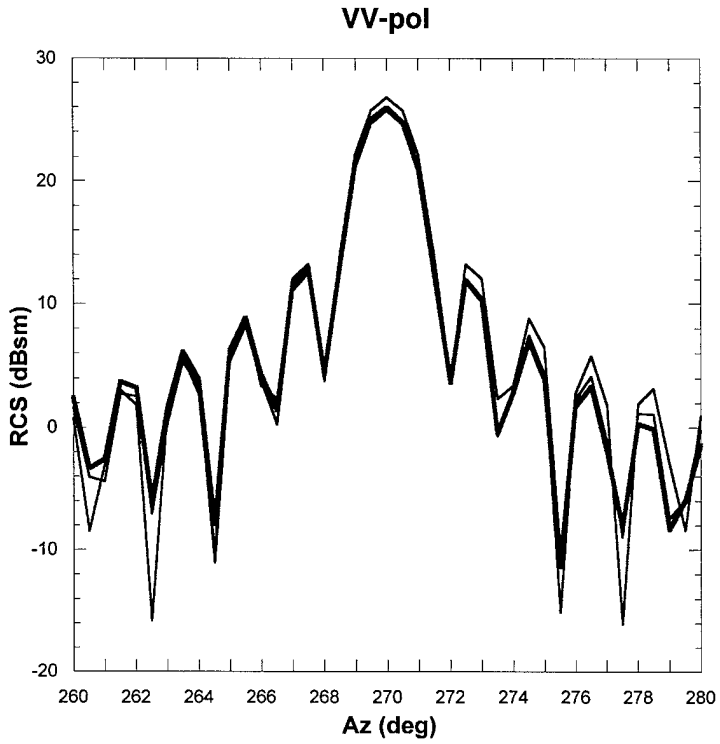

Fig. 22. Shadow boundary influence in forward scattering region for the pencil geometry. The shadow boundary contribution provides a significant correction at the purely forward scattering direction ($Az = 270^{o}$)

E. Summary

The TW-ILDCs significantly improve the calculation of the scattering from bodies with edges. Singularities in the current integration associated with the previous wedge ILDC formulation have been removed, and discontinuities that were present in the calculated scattered field are no longer present. The method partially takes into account second order diffraction effects. The TW-ILDCs derivation includes cross-polarization terms and improves reciprocity.

IV. GEOMETRY TOOL DEVELOPMENT

A. Introduction

The existing edge and ILDC capabilities in ModelMan® have been extended to handle wedge face definitions appropriate for truncated wedge ILDC analyses in Xpatch®. A simple, visual interface has been developed for automatically creating, modifying, and deleting a variety of indexed wedge face definitions. Wedge face definitions can be defined via three methods (i) direct calculations by built-in routines, (ii) import from existing edge files, or (iii) manual entry by the user. Wedge face definitions are included by default when ModelMan® saves an edge file.

B. Graphical User Interface Features

Shown in Fig. 23 is the ModelMan® Wedge Faces tab. This basic operations available through this tab are similar to those of the classical edges but are extended to include settings unique to truncated wedge faces. The functions of this tab are tabulated below:

Visibility – view individual wedge faces by index, usually for manual customization or deletion (see below), or all wedge faces that would be exported.

Show – in the viewer, show representations of any combination of the wedge faces, edges not associated with any wedge face, and faceted geometry.

Settings – sliders for automatic generation of wedge faces. Wedge angle defines minimum angle between adjacent faces, and planar tolerance defines the maximum angle between adjacent facets on the same face. Generation of the wedge faces is dynamically shown in the viewer as the sliders are moved. The sum of the two angles is not allowed to exceed 180.

Selection Options – allows manual customization of wedge faces. Once automatic generation of wedge faces is done per above, individual edges can be removed from or added to the current face by picking on them in the viewer. Edges are not allowed to belong to more than two faces.

Buttons – Add New Face - adds a new indexed face that the user can manually populate with edges. Delete Current Face – deletes the current wedge face definition, leaving the edges to be associated with other wedge faces if desired.

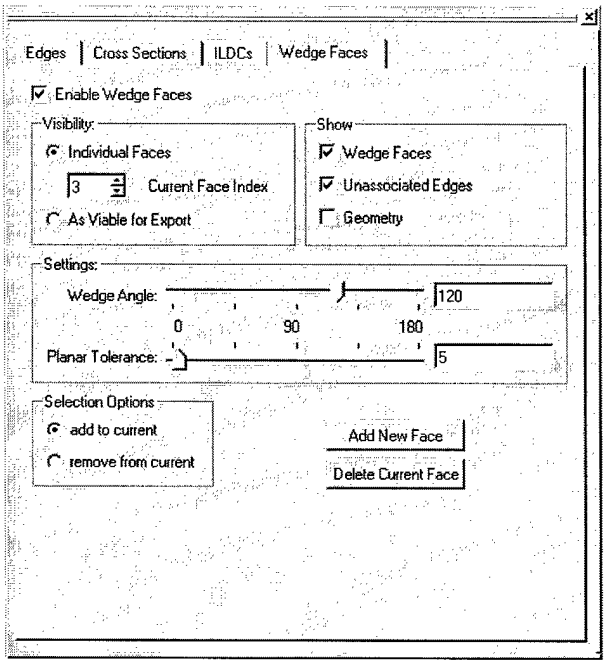

Fig. 23. The ModelMan® Wedge Faces tab. Controls for visibility, filtering tolerances, and selection of wedges are provided for through this interface.

A sample geometry containing multiple edges is shown in Fig. 24. The wedge face tab is employed to identify candidate wedge faces. In the case of automatic wedge face identification, the user has the option to disallow any wedge faces which are deemed unacceptable (such as cases arising from gaps and joints which give rise to fictitious edges). Shown in Fig. 25 are the outlines of the wedge faces corresponding to the original geometry of Fig. 24.

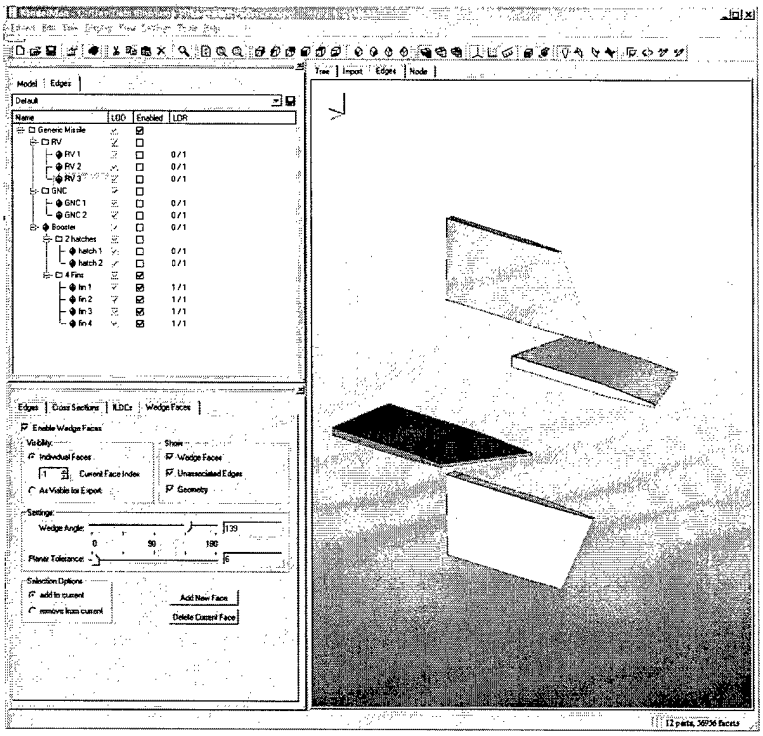

Fig. 24. ModelMan® display for a set of facets illustrating the wedge face associations. On the left is a hierarchical tree indicating parts containing the facets, edges, and associations.

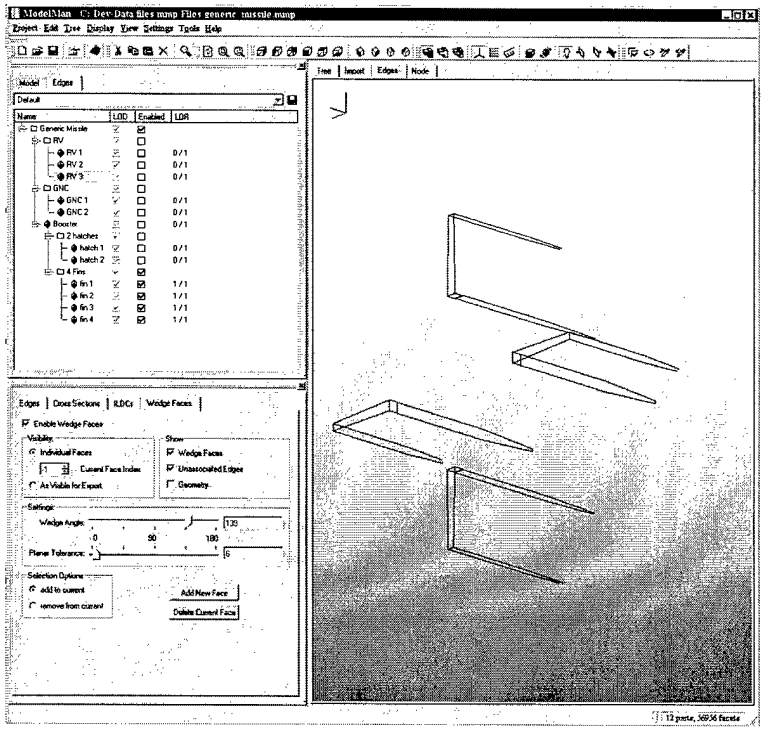

Fig. 25. The individual segments defining each wedge face of the original geometry shown in Fig. 24. This view allows the user to identify and correct incomplete or erroneous wedge face associations.

V. SHADOW BOUNDARY AND CREEPING WAVE STUDY

A. Introduction

One of the key assumptions in the development of the shadow boundary incremental length diffraction coefficients (SB-ILDCs) is the truncation of the creeping wave in the deep shadow region. As identified previously, the SB-ILDCs are not a complete solution to capturing the physics associated with the shadow region, but they nonetheless represent a significant improvement over the physical optics formulation.

In this component of the project, we studied practical techniques for overcoming this deficiency of SB-ILDCs. In particular, techniques were investigated for extending creeping wave rays from the shadow boundary (SB) through surface ray tracing on arbitrary shapes and computing associated surface currents to augment the first-bounce PO solution in Xpatch®. This correction is particularly important for the prediction of time-domain radar signatures and SAR images on smooth targets, since energy can propagate around the target into the deep shadow region and back into the lit region, generating delayed response features that are missing in the SB-ILDC formulation.

In executing this work, a research code developed at the University of Kentucky was employed to accelerate progress on the studies. This code also implements a novel solution to the identification of SBs on smooth targets. As part of this work, we studied the specifics and performance of this SB-finding algorithm and have compared it to the practical algorithm based on ray tracing developed for the incorporation of SB-ILDCs into Xpatch®.

In electromagnetic scattering problems, the PO method is a quick way of determining the surface currents on the scattering body without the need to rigorously solve Maxwell's equations. This method is generally suitable when the target and key target features are electrically large. In practice, target features on the order of a wavelength still do very well with the PO approximation, and larger features perform even better.

One of the well-known anomalies of PO is that it only predicts reasonable surface currents in the lit region of the target, while non-physically yielding zero surface currents on surfaces blocked from direct illumination. In other words, the PO surface currents abruptly end at the shadow boundary (SB) of the target (with respect to the source), even if the target surface is smooth in the vicinity of the SB. Among other problems, this creates a non-physical scattering feature, which can be observed and localized to the SB in the time-domain scattering response. In reality, the surface currents should smoothly transition in crossing the SB from the lit side to the dark side. Once in the dark side, the surface currents should rapidly decrease as they shed energy to free space since they are not reinforced through direct illumination.

The effect is illustrated in Fig. 26, which gives the time-domain monostatic backscattering of a PEC sphere (radius $a = 0.0477\ m$) based on the exact solution to Maxwell's equations (Mie Series [2]) and the PO approximation. In the figure, the time-axis has been replaced with down range distance using the usual technique of mapping the monostatic response time delays to one-dimensional positions on the target along the incident / back-scatter axis. The initial response at

$z = -a = -0.048$ *m* corresponds to the leading edge of the sphere, and here PO and the exact solution are in excellent agreement. Agreement on this critical feature in the time response summarizes in a special case the popularity of the PO approximation for general scattering problems where exact solutions are not available. However, beyond this leading edge response, the exact and PO solutions markedly diverge, albeit at somewhat lower levels than the initial response. First, the PO response at down range position $z = 0$ is the spurious scattering feature introduced by the abrupt and non-physical termination of surface currents at the sphere SB. Second, the exact solution contains a delayed response at $z = \pi a/2 = 0.075$ *m* that is completely absent from the PO solution. This is caused by surface tangential creeping waves that originate from the shadow boundary and travel around the sphere along its meridians.

The creeping waves constantly shed energy to space in their direction of travel, and when they again reach the SB on the opposite side of the sphere from where they started, their radiation is directly in the back-scattering (monostatic) direction. This also means that creeping waves can play a significant role in bistatic scattering at observation angles where the specular (PO) scattering mechanisms are weak.

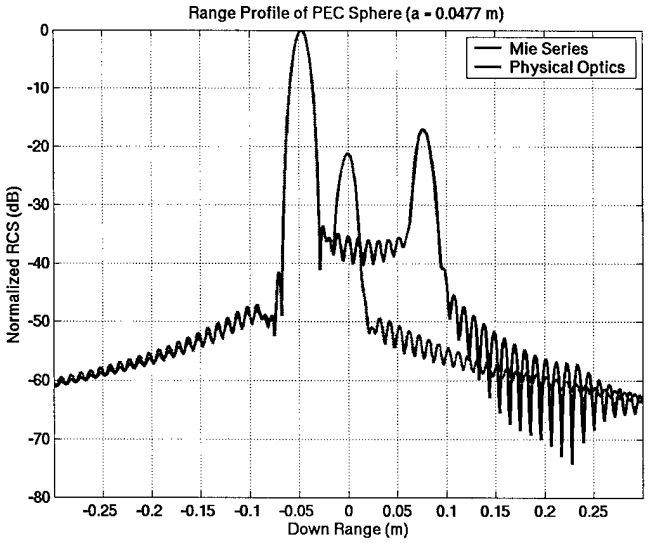

Fig. 26. Monostatic time-domain response (range profile) of PEC sphere ($a = 0.0477$ *m*): physical optics and Mie series solutions. Note the erroneous late time responses in the red PO curve due to (a) discontinuous PO fields at the shadow boundary and (b) omission of creeping waves traveling in the deep shadow.

The effect of the discrepancy between PO and the exact solution for the PEC sphere can also be observed in the frequency response, as shown in Fig. 27. At higher frequencies ($k_0 a >> \lambda$), PO and the exact solution converge to the same RCS level, and this is to be expected from an asymptotic solution like PO. However, the variation of the response with frequency as modeled by PO is incorrect, and this can be attributed to both poor approximation of surface currents in the vicinity of the SB and the complete absence of deep shadow surface currents associated with the creeping wave mechanism

B. Technical Overview

The core methodology of Xpatch® is the shooting-and-bouncing ray (SBR) method, which extends the 1st-bounce PO solution to multi-bounce through geometrical optics (GO) ray tracing and successive application of PO to approximate surface currents beyond the 1st-bounce according to the incident and reflected GO fields.

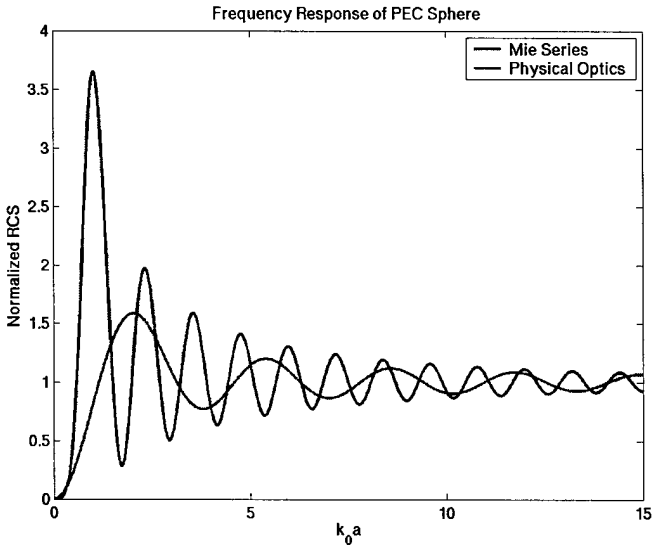

Fig. 27. Monostatic frequency response of PEC sphere: physical optics and Mie series solutions. Note that shadow boundary ILDCs will provide improvements to the PO for $ka > 6$ (see Fig. 8).

More abstractly speaking, Xpatch® seeks to predict electromagnetic scattering, and associated effects of specular reflection and diffraction, through an asymptotic approximation of surface currents on complex targets. While Xpatch® employs geometric ray tracing to approximate the currents, the terminal point (or escape direction) of tracked rays is not considered in establishing the dominant directions of scattered energy. Rather, it relies on the radiated wave interference of the approximated surface currents to reconstruct the spatial and angular regions of strong scattering. In this respect, SBR corresponds to the actual (physical) process of scattering. One of the benefits of this approach is that complex and arbitrary scattering geometries can be handled readily without the need to search for dominant, geometrically minimized ray paths terminating at or near scattering angles of interest. In developing a technique for handling the deep shadow region in Xpatch®, we have sought to evaluate an approach that is consistent with the underlying surface current approximation framework of Xpatch®. To that end, the technical approach can be summarized as follows:

1) Identify the SB on the target.
2) Sample the SB uniformly at sub-wavelength intervals.
3) Launch tangential creeping waves from the SB into the shadow region.
4) Trace the creeping waves over smooth target surfaces to form geodesics (*i.e.*, paths that locally minimize path length as they extend).
5) Generate surface currents associated with the found creeping wave paths.

6) Radiate these surface currents to space and combine the result with the base Xpatch® PO-SBR solution.

1. Finding the Shadow Boundary (Alternate Method)

By definition, the shadow boundary is the locus of illuminated points on the target where $\hat{n} \cdot \bar{k}_{inc} = 0$, which we refer to has the incident-normal dot product. The research code employed in these studies implements an algorithmic Method B for finding the shadow boundary that is somewhat different from the algorithmic Method A presented earlier in the SB-ILDC component of this project.

Both Methods A and B are intended for targets described by curved surfaces. Without going into great detail since it has already been presented, Method A employs an exhaustive search by looping through the curved surfaces comprising the target and subdividing them into small patches, nominally 0.1 λ on a side. Each small patch is nearly planar and has four sides and four corners. The incident-normal dot product is computed for each of the four corners. Based on the signs of these dot products, it can be established whether the SB intersects the patch. If it does, the approximate path of the SB across the patch can be established through linear interpolation.

Method B is based on the observation that the SB forms a closed curve along the geometry of the surface. Method B consists of two-steps:

1) Find one point on the target along the SB. This point designates the SB start point.
2) Extend the SB curve along the target surface in small incremental steps. Repeat step 2 and stop when the SB closes back on itself at the start point.

To find an SB start point, all the curved surfaces comprising the target are subdivided, with the limited objective of yielding mildly curved, quad patches that do not fold back on themselves. A 4 x 4 subdivision is usually adequate. The algorithm then loops through these patches until one is found with a side that intersects the SB. This determination is made using the same technique as in Method A of testing the incident-normal dot product at each corner of the patch. A sign change in the dot product indicates an SB intersection with the side bounded by the two corners. The precise location of the SB along the side is then determined by uniformly sampling the dot product along the side and further localizing the dot product zero-crossing through linear interpolation. This yields an SB start point on the "start patch," referred to as *SB-P1* (Shadow Boundary Point 1). The sampling and interpolation process is more conveniently implemented in the 2-D parameterized space of the patch domain (*i.e.*, *u,v* coordinates) rather than directly in the 3-D target CAD space of patch range (*i.e.*, *x,y,z* Cartesian coordinates).

If the SB intersects one side of a patch, it must intersect another side as well at *SB-P2*, as shown in Fig. 28. This second side is identified through the dot product sign testing. The SB intersection with the second side is then localized to *SB-P2* as before. Having established *SB-P1* and *SB-P2* on the patch sides, the SB can now be extend through the patch from *SB-P1* on the first side and toward *SB-P2* on the second side. In the implementation utilized during this study, the SB contour was approximated as cutting a linear path in the 2-D parameterized domain space

of the patch, and this was found to be adequate for all test cases. While higher-order (*i.e.*, more accurate) means of extending the SB through the patch can be developed, the same result can be achieved by employing finer subdivisions in the piecewise linear approach presented above. Regardless, the present approach yields many SB points over the patch, forming a curved 1-D path in the 3-D target geometry space. These patch interior SB points are not enumerated in the notation here, but they are collected consecutively in the algorithm.

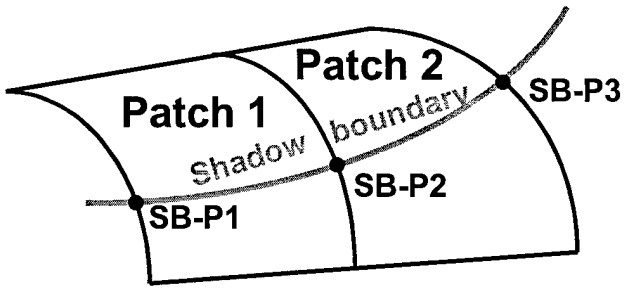

Fig. 28. Illustration of Method B for finding the shadow boundary. The result of Method B is a contiguous shadow boundary spanning entire patches and encircling the entire geometry.

Having established the SB contour along a single patch in the target, the next step is to extend the SB to the neighboring patch that shares the same side containing *SB-P2* on the first patch. This can be reliably achieved with a topologic map of the target geometry patches. The mapping establishes connectivity along the fours sides of each patch with its neighboring patches. Details of the construction of the topologic map will be presented later. Once the first side of the neighbor patch is identified, *SB-P2* is carried over by appropriate conversion of the parameter coordinates (u,v) from the first patch to the second patch.

At this point, the Method B algorithm is now in exactly the same state for *SB-P2* on the second patch as it found itself after having identified *SB-P1* on the first patch. Hence the process can be repeated, and the SB extended across the target geometry from patch to patch. The process completes when the extended SB closes back on *SB-P1*.

An example of the results of this algorithm are shown in Fig. 29. After the SB has been constructed as a list of points, it can be uniformly re-sampled through a spline fit to achieve any desired density of points. This is useful in establishing launch points for creeping wave rays of uniform width, as discussed later. The whole process proves to be computationally efficient. For the example given in Fig. 29, on the order of a CPU second was required to establish the SB.

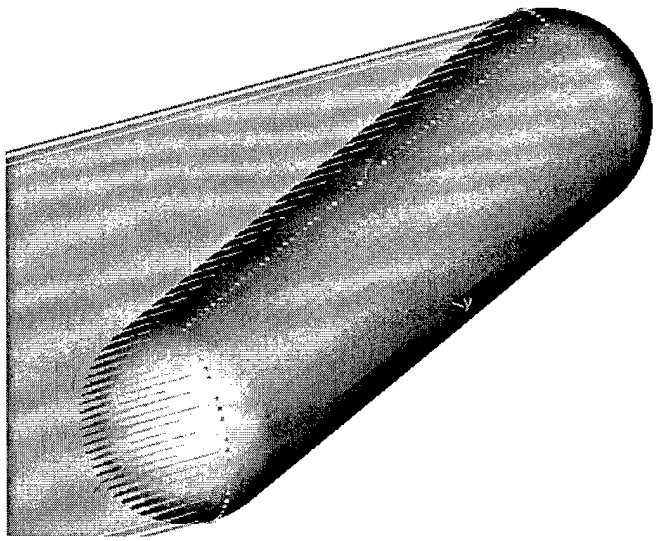

Fig. 29. Shadow boundary (colored points) found by the alternate Method B on a cylinder with hemisphere end caps. The incident angles is 60° off the cylinder broadside. The incident far field ray trace is also shown to illustrate the consistency of the extracted SB with the boundary of the incident ray field on the target.

As mentioned, continuing the shadow boundary from one curved surface patch to the next is effected through a topological map. This map can be built once, after the original subdivision of the target curved surfaces into smaller patches. In the code used for this study, the topologic map was constructed by evaluating the 3-D position of the corners on all the patches and finding matches among these corners. By allowing a small tolerance in matching the corners, it is not necessary for the sides of neighboring patches to perfectly align. This is an important consideration since target models based on curved surfaces often suffer from this problem to some degree.

In the examples we considered, all of the surface patches aligned with neighbors at their quad corners. In practical target CAD models, it is common to encounter patches that share a portion of their side without sharing a corner (*i.e.*, the corner of one patch resides in the middle of a side of its neighbor patch). In this case, corner matching will not work in constructing the topology map, and more rigorous search techniques are required. One practical possibility is to use a geometric ray tracer to systematically interrogate the space in the immediate vicinity around the patch sides. This process will construct a complete list of all neighboring patch relations and can then used to expedite the construction of the topology map. As with the corner-matching approach, the more rigorous ray tracing approach to identifying neighbor patch connectivity can be implemented with a small spatial tolerance to allow for inadvertent gaps between patches.

2. Qualitative Comparison of Shadow Boundary Search Method

Having described two methods for finding the SB, we now compare their relative merits. Method A, based on exhaustive search, has the benefit of inherent robustness. On a complex target, it will find all the shadow boundaries. In contrast, Method B, as described, will only find one of the contiguous SBs. This is because it starts by finding one SB point and then extending the SB curve until it closes on itself. On all but simple convex targets, there are multiple SB

contours. This does not eliminate Method B and instead suggests some mechanism must be added to seed the multiple SBs.

Method B, based on seeding an SB and extending it to closure, has the advantage of automatically yielding a contiguous shadow boundary. In contrast, Method A produces disjoint samples of the SB. For implementation of the SB-ILDCs, this is not an issue, but it would be a problem in launching creeping wave rays in a spatially controlled fashion. This does not eliminate Method A from the creeping wave application, but it means some mechanism must be added by which the disjoint points can be grouped in to one or more contiguous SBs to facilitate uniform re-sampling.

Finally, with Method A, the computational effort is proportional to the surface area of the target measured in wavelengths squared. In contrast, with Method B, the computational effort is proportional to a combination of the number of target model patches and the length of the shadow boundary contours. In terms of computational scaling, Method B would appear to be better. However, this does not mean that Method B will always be faster than Method A. It just means that for a large enough problem size, Method B should be faster than Method A. The actual performance of these methods has not been tested at this reporting, so no conclusions beyond scaling properties are made at this time.

In closing, we mentioned earlier that Method B would require some means of seeding multiple SBs on a practical target. One possibility is to construct the first SB and then begin the process all over, searching through the patches to find another incident-normal dot product zero-crossing. Instead of stopping automatically on first zero-crossing, the search continues until a patch side zero-crossing is found that is not already part of an existing SB contour. On the final iteration, the search will yield no zero-crossings that are not previously covered, indicating that all SBs have been found. An implementation of this approach appears practical, but whether or not it would be reliable has not been tested.

C. Method for Tracing Creeping Waves

As described previously, the motivation for this component of the project is to evaluate practical means of obtaining surface currents in the deep shadow region of targets by including a creeping wave mechanism to predict the deep shadow surface currents. This requires launching creeping wave rays from the shadow boundary and tracing them on the target surface into the shadow region, possibly traveling far enough to emerge back into the lit region on some other part of the target. The intent is to use the creeping rays paths as domains for creeping wave surface currents, which are themselves propagated according to the geometrical properties of the creeping rays and the underlying surface.

The launch points are established by uniformly sampling the target SBs, as discussed earlier. The launch direction is the direction of the incident wave at the SBs, which by definition is tangent to the target surface. As required by the asymptotic creeping wave physics, to continue the rays along the target surface, they must maintain a geodesic path. Any 1-D arc conformal to a smooth 2-D surface and occupying a 3-D space has the property of arc length, which is simply the

distance traversed along the arc. For a geodesic path between two end points with arc length s_0, any small, surface-conformal perturbation of the arc between the end points would yield a new arc length $s_0 + \delta s$, where $\delta s > 0$. This is the definition of a geodesic curve [10,11].

The concept of a geodesic arc is simple. Differential equations for tracing one along an arbitrary curved surface are somewhat more complicated but, in the end, manageable in a numerical implementation. For a curved surface patch, the 3-D displacement vector, $\boldsymbol{r}$, to a point on the surface is parameterized in 2-D u,v coordinates: $\boldsymbol{r} = \boldsymbol{r}(u,v)$. As shown in Fig. 30, the numerical geodesic tracing problem is as follows: given point $P_0(u_0,v_0)$ on the surface and initial direction $\hat{t}_0$ tangent to the surface, advance the curve to unknown point $P_N(u_N,v_N)$ by taking small steps Δu, Δv (also unknown) while maintaining a geodesic path at all points along the way. To be clear, although the geodesic path resides in 3-D target geometry space, it will be advanced through operations in parameterized 2-D u,v space.

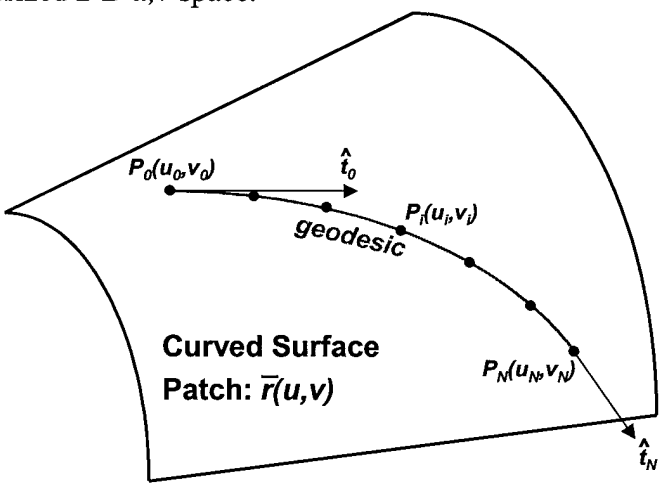

Fig. 30. A geodesic path started at known point P_0 in known direction $\hat{t}_0$ and numerically advanced through small incremental steps.

Since the 1-D geodesic arc lies on the 2-D surface, any point along the arc can be expressed in u,v coordinates, but u and v are not independent variables along the 1-D arc. The approach for forming the geodesic arc is to numerically solve the differential equations relating the u and v. These equations are given by [10,11] as

$$\frac{d^2u}{dv^2} = \Gamma_{11}^2\left(\frac{du}{dv}\right)^3 + \left(2\Gamma_{12}^2 - \Gamma_{11}^1\right)\left(\frac{du}{dv}\right)^2 + \left(\Gamma_{22}^2 - 2\Gamma_{12}^1\right)\frac{du}{dv} - \Gamma_{22}^1 \tag{16}$$

and

$$\frac{d^2v}{du^2} = \Gamma_{22}^1\left(\frac{dv}{du}\right)^3 + \left(2\Gamma_{12}^1 - \Gamma_{22}^2\right)\left(\frac{dv}{du}\right)^2 + \left(\Gamma_{11}^1 - 2\Gamma_{12}^2\right)\frac{dv}{du} - \Gamma_{11}^2. \tag{17}$$

The coefficients Γ^1_{12}, Γ^2_{11}, *etc.* (called Christoffel symbols) relate to differential properties of the 2-D surface and are given later. These values can be determined directly from the algebraic expressions for ***r(u,v)*** for the surface patch. At any given point, only one of these two equations needs to be solved, the choice depending on the current state *du/dv* and stability considerations.

From $\hat{t}_0$, one can determine du_0/dv_0, as will be explained shortly. Let us assume that $du_0/dv_0 < 1$ for now. Also, we can scale Δu_0 and Δv_0 to correspond to the desired step size in 3-D space, Δs_0. This yields four parameters for P_0: u_0, v_0, Δu_0, Δv_0.

From (16), d^2u/dv^2 at P_0:$u_0,v_0,\Delta u_0,\Delta v_0$ is determined through direct substitution. Implementing the 2nd-order Euler method, we obtain

$$u_1 = u_0 + \Delta u_0, \tag{18a}$$

$$v_1 = v_0 + \Delta v_0, \tag{18b}$$

$$\Delta u_1 = \Delta u_0 + \frac{d^2u}{dv^2}\Big|_{u0,v0} (\Delta v_0)^2, \tag{18c}$$

$$\Delta v_1 = \Delta v_0. \tag{18d}$$

The general iteration becomes

$$u_{i+1} = u_i + \Delta u_i, \tag{19a}$$

$$v_{i+1} = v_i + \Delta v_i, \tag{19b}$$

$$\Delta u_{i+1} = \Delta u_i + \frac{d^2u}{dv^2}\Big|_{ui,vi} (\Delta v_i)^2, \tag{19c}$$

$$\Delta v_{i+1} = \Delta v_i. \tag{19d}$$

Proceeding in this way, it may happen that $\Delta u_i > \Delta v_i$ (*i.e.*, $\Delta u_i/\Delta v_i < 1$) for some *i*. When this occurs, numeric stability is enhanced by switching to (17) and iterating as

$$u_{i+1} = u_i + \Delta u_i, \tag{20a}$$

$$v_{i+1} = v_i + \Delta v_i, \tag{20b}$$

$$\Delta u_{i+1} = \Delta u_i, \tag{20c}$$

$$\Delta v_{i+1} = \Delta v_i + \frac{d^2v}{du^2}\Big|_{ui,vi} (\Delta u_i)^2. \tag{20d}$$

Higher-order numeric iteration solutions to the differential equations of (16) and (17) may also be implemented to improve accuracy or allow a larger step size with each iteration, but the 2nd-order Euler is the simplest.

The original du_0/dv_0 at P_0 can be obtained from $\hat{t}_0$ in the following manner. For a 1-D arc conformal to the surface and parameterized as $\boldsymbol{r} = \boldsymbol{r}(u,v) = \boldsymbol{r}(u(t),v(t))$, the tangent velocity vector is given by

$$\bar{t} = \frac{d\bar{r}}{dt} = \bar{r}_u \frac{du}{dt} + \bar{r}_v \frac{dv}{dt}. \tag{21}$$

Here, we use the notation $\boldsymbol{r}_u = \partial\boldsymbol{r}/\partial u$, $\boldsymbol{r}_v = \partial\boldsymbol{r}/\partial v$ to express the unit tangent vector $\bar{t}$ as

$$\bar{t} = t_1\bar{r}_u + t_2\bar{r}_v, \tag{22}$$

where

$$\frac{t_1}{t_2} = \frac{du}{dv}. \tag{23}$$

Taking the dot product of (22) with $\boldsymbol{r}_u$ and $\mathbf{r}_v$, respectively, we obtain

$$\begin{bmatrix} E & F \\ F & G \end{bmatrix}\begin{bmatrix} t_1 \\ t_2 \end{bmatrix} = \begin{bmatrix} \hat{t}\cdot\bar{r}_u \\ \hat{t}\cdot\bar{r}_v \end{bmatrix}, \tag{24}$$

where

$$E = \bar{r}_u\cdot\bar{r}_u,\ F = \bar{r}_u\cdot\bar{r}_v,\ G = \bar{r}_v\cdot\bar{r}_v. \tag{25}$$

From (23) and (24), we then obtain

$$\frac{du}{dv} = \frac{G\left(\hat{t}\cdot\bar{r}_u\right) - F\left(\hat{t}\cdot\bar{r}_v\right)}{E\left(\hat{t}\cdot\bar{r}_v\right) - F\left(\hat{t}\cdot\bar{r}_u\right)}. \tag{26}$$

If this yields $du/dv < 1$, then the reciprocal dv/du should be used to initiate the iteration process with (17) instead of (16). Regardless, knowledge of the ratio from (26) that is consistent with movement along the arc in the $\pm\hat{t}_0$ direction allows setting of Δu_0 and Δv_0 to achieve the desired step size, $|\Delta\boldsymbol{r}_0| = \Delta s_0$. The incremental step in 3-D target space is given by

$$\Delta\bar{r} \cong \bar{r}_u\Delta u + \bar{r}_v\Delta v, \tag{27}$$

which yields,

$$(\Delta s)^2 = \Delta\bar{r}\cdot\Delta\bar{r} = E(\Delta u)^2 + 2F\Delta u\Delta v + G(\Delta v)^2. \tag{28}$$

Next, setting $\Delta u/\Delta v = du/dv$ or $\Delta v/\Delta u = dv/du$ results in

$$\Delta v = \pm\frac{\Delta s}{\sqrt{E\left(\frac{du}{dv}\right)^2 + 2F\frac{du}{dv} + G}} \tag{29a}$$

or

$$\Delta u = \pm \frac{\Delta s}{\sqrt{E + 2F\frac{dv}{du} + G\left(\frac{dv}{du}\right)^2}}. \tag{29b}$$

Finally, select the sign for Δv (or Δu) to correspond to the sign for t_2 (or t_1) obtained from (24). As the iteration progresses, arc step size Δs_i will stray from the original and desired Δs_0. This is corrected by rescaling Δu_i and Δv_i after each iteration to maintain Δs_0. Smaller Δs improves the accuracy of the numerical solution to the differential equation.

The Christoffel symbol coefficients [10,11] in (16) and (17) follow:

$$\Gamma_{11}^1 = \frac{GE_u - 2FF_u + FE_v}{2\Delta},\ \Gamma_{11}^2 = \frac{2EF_u - EE_v - FE_u}{2\Delta}, \tag{30a}$$

$$\Gamma_{12}^1 = \frac{GE_v - FG_u}{2\Delta},\ \Gamma_{12}^2 = \frac{EG_u - FE_v}{2\Delta}, \tag{30b}$$

$$\Gamma_{22}^1 = \frac{2GF_v - GG_u + FG_v}{2\Delta},\ \Gamma_{22}^2 = \frac{EG_v - 2FF_v - FG_u}{2\Delta}, \tag{30c}$$

$$\Delta = EG - F^2, \tag{30d}$$

where $E_u = \partial E/\partial u$, etc.

The above procedure will track a geodesic across a single patch symbolically and parametrically specified by $\boldsymbol{r} = \boldsymbol{r}(u,v)$. When the geodesic reaches the edge of a patch, it is necessary to continue the geodesic into the bordering patch. This can be achieved using the topology map in a manner similar to that described for extending the SB path across patch borders.

Figure 31 illustrates the implementation of the creeping wave ray tracer on a cylinder with hemisphere end caps. The creeping rays emanate from the SB in the direction of the incident wave. On this geometry, one can observe the formation of both caustic points and the more general caustic arcs (lines). This issue of creeping wave caustics is discussed below. Note also that some creeping rays emerge back into the lit side after traveling around the shadow side. For backscattering applications, these rays can generate significant delayed scattering features on smooth bodies.

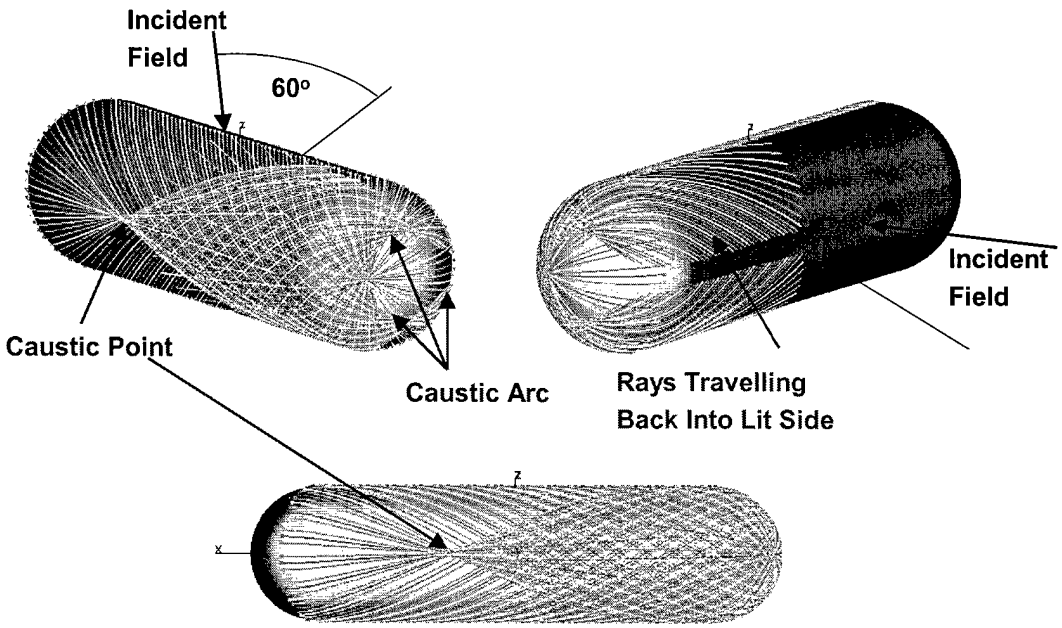

Fig. 31. Traced creeping wave rays on a cylinder with hemisphere end caps. The creeping wave ray paths are plotted without regard to energy decay along the geodesic paths.

The next section will discuss the means of assigning proper creeping wave surface currents to the creeping rays, but a few geometrical points remain to be addressed. The creeping rays are 1-D arcs, but what is required for a scattering computation are creeping ray "tubes" which are 2-D ribbons over the surface. One way to obtain these is to consider two creeping ray arcs launched from neighboring points on the SB separated by a sub-wavelength distance (*e.g.*, $\lambda/10$). The two arcs then define the lateral boundaries of a creeping wave ray tube. Depending on local surface curvature conditions encountered as these geodesic arcs are constructed, the ray tube walls will either converge or diverge. When traveling over flat surfaces, or even singly curved surfaces (*e.g.*, cylindrical surfaces), the divergence rate remains fixed. On general, doubly curved surfaces (*e.g.*, sphere, ellipsoid, *etc.*), divergence rate varies as the ray tube propagates. These effects can also be observed in Fig. 31.

One of the critical geometrical properties required in evaluating the surface currents is the divergence factor of the creeping wave ray tube. This can be obtained directly by measuring the lateral separation between the creeping ray walls at any point along their respective arcs. This separation must be determined at points of common arc length (measured from the SB) between the two geodesic arcs. The divergence factor is given by

$$D = \sqrt{\frac{W_0}{W_i}}, \tag{31}$$

where W_i is the ray tube lateral width at the creeping ray sample point and W_0 is the original width at the SB.

Two other geometrical quantities are required by the creeping wave formulation: arc curvature and arc torsion. The arc curvature at any point along the geodesic is given by [10]

$$\mathrm{K}_{arc} = \frac{et_1^2 + 2ft_1t_2 + gt_2^2}{Et_1^2 + 2Ft_1t_2 + Gt_2^2}, \tag{32}$$

where t1 and t2 are obtained from (24). Since t1 and t2 are also proportional to Δu and Δv, these can be substituted directly into (32) to yield K_{arc} as the geodesics are constructed. The coefficients E, F and G are given in (25). The coefficients e, f, and g are given by

$$e = \bar{r}_{uu} \cdot \hat{n},\ f = \bar{r}_{uv} \cdot \hat{n},\ g = \bar{r}_{vv} \cdot \hat{n}, \tag{33}$$

where $\hat{n}$ is the 2-D surface normal and $\boldsymbol{r}_{uu} = \partial^2\boldsymbol{r}/\partial u^2$, *etc.*

The formulation also requires the arc torsion at the SB launch point of the creeping ray. This is given by

$$T = \sqrt{\left|(\mathrm{K}_{arc} - \mathrm{K}_1)(\mathrm{K}_2 - \mathrm{K}_{arc})\right|}, \tag{34}$$

where K_1 and K_2 are the principal curvatures of the surface. They are the two roots of the quadratic equation,

$$\mathrm{K}^2 - 2\mathrm{K}_m\mathrm{K} + \mathrm{K}_g = 0, \tag{35}$$

where

$$\mathrm{K}_m = \frac{eG - 2fF + gE}{2\left(EG - F^2\right)}, \tag{36a}$$

$$\mathrm{K}_g = \frac{eg - f^2}{EG - F^2}. \tag{36b}$$

K_m and K_g are termed the mean surface curvature and Gaussian surface curvature, respectively.

D. Method for Determining Creeping Wave Surface Currents

Direct asymptotic solutions for surface currents in the shadow region (and the transition region around the SB) are not available. However, researchers [12, 13] have developed workable formulations for arbitrary convex surfaces by heuristically combining asymptotic solutions to the canonical problems of metallic sphere and cylinder scattering [2,14]. The sphere is a doubly curved surface with creeping rays that converge toward a caustic in the deep shadow region and then diverge again. The cylinder is a singly curved surface with non-diverging creeping waves that also introduces the effect of torsion at oblique incidence angles. Hence, these two canonical solutions, together, incorporate the key physical effects for a heuristically constructed general solution.

1. Fock Creeping Wave Solution for a Sphere

To anticipate the benefit of this approach, we studied scattering based on the creeping wave formulation for the PEC sphere (radius a), one of the canonical components in the generalized heuristic formulation. For this case, we assume a plane wave incident in the $-z$ direction with a unit electric field polarized in the $+x$ direction, as shown in Fig. 32.

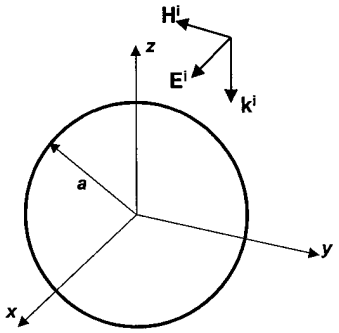

Fig. 32. Incident plane wave and polarization for the sphere scatterer. The incident direction is directly toward the sphere's north pole, and the shadow boundary will be the equator defined along the xy-plane.

The total magnetic evaluated at the sphere surface ($r = a$) is given by [2,13,14] $\overline{H} = H_\theta \hat{\theta} + H_\phi \hat{\phi}$, with

$$H_\theta = \frac{-jD}{m}\left[c_0 e^{jk\tau_1} f(\xi_1) - je^{jk\tau_2} f(\xi_2)\right] + \frac{jD^3}{ka}\left[c_0^3 e^{jk\tau_1} g(\xi_1) + je^{jk\tau_2} g(\xi_2)\right] \tag{37a}$$

and

$$H_\phi = -D\left[c_0 e^{jk\tau_1} g(\xi_1) - je^{jk\tau_2} g(\xi_2)\right] - \frac{D^3}{kam}\left[c_0^3 e^{jk\tau_1} f(\xi_1) + je^{jk\tau_2} f(\xi_2)\right], \tag{37b}$$

where $0 < \theta < \pi$ and

$$D = \frac{1}{\sqrt{\sin\theta}}, \tag{38a}$$

$$c0 = \begin{cases} 1 & ,\pi/2 \le \theta \le \pi \text{ (shadow region)} \\ 1/D & ,0 \le \theta \le \pi/2 \text{ (lit region)} \end{cases}, \tag{38b}$$

$$m = \left(\frac{ka}{2}\right)^{1/3}, \tag{38c}$$

$$\tau_1 = \begin{cases} a(\theta - \pi/2) & ,\text{shadow region} \\ -a\cos\theta - \xi_1^3/3k & ,\text{lit region} \end{cases}, \tag{38d}$$

$$\xi_1 = \begin{cases} m\tau_1/a & ,\text{shadow region} \\ -m\cos\theta & ,\text{lit region} \end{cases}, \tag{38e}$$

$$\tau_2 = a(3\pi/2 - \theta), \tag{38f}$$

$$\xi_2 = m\tau_2 / a. \tag{38g}$$

In these expressions, time-harmonic dependence *exp(-jωt)* is assumed throughout. Fock functions $f(\xi)$ and $g(\xi)$ are given by [2,14] as

$$f(\xi) = \frac{1}{\sqrt{\pi}} \int_{\Gamma} \frac{e^{i\xi t}}{w_1(t)} dt, \tag{39a}$$

$$g(\xi) = \frac{1}{\sqrt{\pi}} \int_{\Gamma} \frac{e^{i\xi t}}{w_1'(t)} dt, \tag{39b}$$

Where $w_1(t)$ and its derivative are Fock-type Airy functions. Γ is a complex contour that starts at infinity in the angular sector $\pi/3 < arg\ t < \pi$ and ends at infinity in the angular sector $-\pi/3 < arg\ t < \pi/3$. Along the way, Γ passes between the origin and the pole of the integrand nearest the origin. The properties of $f(\xi)$ and $g(\xi)$ and methods of their evaluation are available from [2,14].

The surface current can be obtained from (37) using $\bar{J} = \hat{n} \times \bar{H}$. Alternatively, using the PO approximation, the surface currents are given by $\bar{J}_{PO} = 2\hat{n} \times \bar{H}^i$. The resulting surface currents for $k_0 a = 3$ are shown in Fig. 33. It is evident that the creeping wave formulation yields more realistic surface currents than PO, with the exception of the singularity at $\theta = \pi$ (the caustic), where the creeping wave formulation is known to break down. The creeping wave formulation also diverges at $\theta = 0$ due to the caustic for the creeping wave traveling around the back side and re-emerging into the lit region, although the effect is less pronounced since the underlying creeping wave has traveled twice as far as the distance to the first caustic.

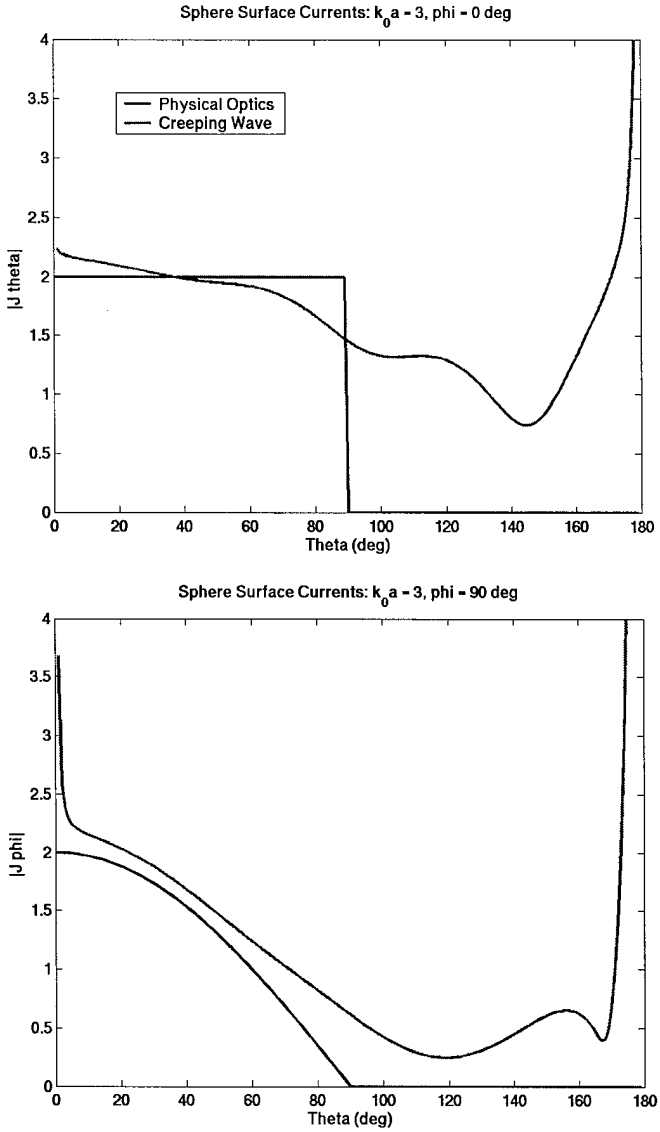

Fig. 33. Surface currents on sphere predicted by physical optics and creeping wave formulation: (a) $|J_\theta|$ at $\phi=0$, (b) $|J_\phi|$ at $\phi=\pi/2$. Note that the influence of the caustic points at the sphere's poles has not been removed in these plots.

The back-scattered field radiated by the surface currents is given in Fig. 34 as a frequency response. This is the same plot as Fig. 27, but this time we include the result for the creeping wave formulation. Clearly, the creeping wave formulation is a significant improvement over PO, using the exact solution Mie series as the reference.

The time domain (range profile) response of the sphere ($a = 0.0477\ m$) in Fig. 35 also shows significant improvement using the creeping wave formulation. The false scattering feature predicted by PO at down range position $z = 0$ has been completely eliminated owing to the uniform expressions for the surface currents current in the vicinity of the SB in (37). Also, the delayed response at $z = \pi a/2 = 0.075\ m$, due to energy traveling around the back side of the sphere and re-emerging on the other side, is also correctly predicted. However, the creeping

wave formulation also introduces a false scattering feature at $z = a(\pi/2 + 1)/2 = 0.061\ m$. This is caused by the breakdown of the formulation in the vicinity of the caustic at $\theta = \pi$.

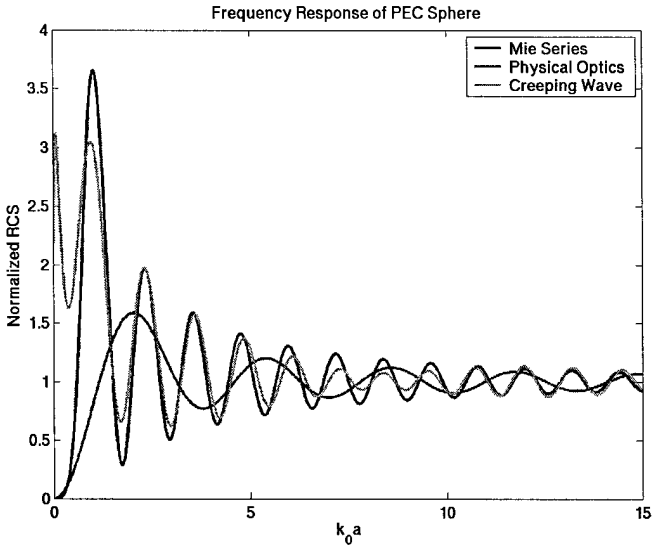

Fig. 34. Frequency back-scattering response of the PEC sphere computed by exact solution (Mie series), asymptotic creeping wave formulation, and physical optics.

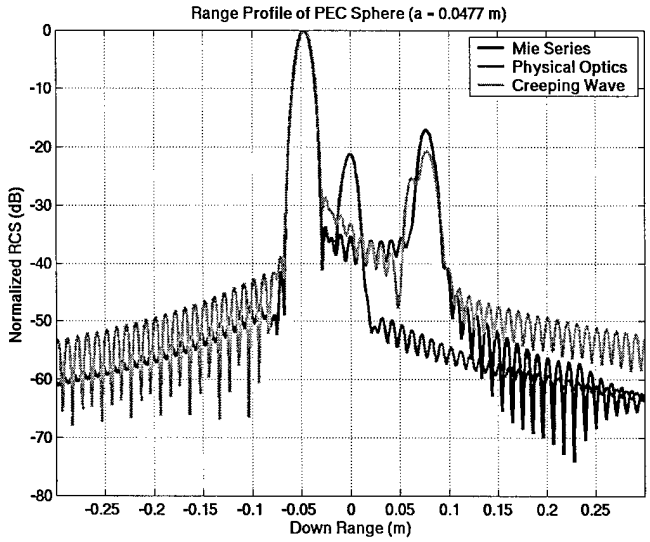

Fig. 35. Time-domain back-scattering response of PEC sphere ($a = 0.0477\ m$) computed by exact solution (Mie series), asymptotic creeping wave formulation, and physical optics.

To keep the surface current radiation integral from diverging, the integration is abruptly terminated at $\theta = 179^o$. This gives a better result than integrating all the way through caustic at $\theta = 180^o$, but a false scattering feature is still generated by the abrupt truncation. There are convergent asymptotic expressions for the surface currents in the vicinity of the caustic on the sphere [2,14], but these do not so readily lend themselves to a generalized solution for arbitrary curved surfaces. In practical problems involving targets with doubly curved surfaces, caustics

will occur, so this problem must be confronted. A practical strategy may be to smooth the currents around the caustic so as to avoid both the caustic singularity and the false scattering features created by abrupt truncation of the radiation integral. At the time of this reporting, however, this approach has not been implemented or tested in our study.

2. General Solution for Creeping Waves in the Shadow Region

For a general creeping wave expressions that can be used with the arbitrary geodesic paths over convex surfaces, it is useful to define a local right-handed coordinate system, $\hat{n},\hat{b},\hat{t}$, for the creeping rays, as shown in Fig. 36. At all points along the geodesic arc, $\hat{n}$ is the outward surface normal, and unit tangent vector $\hat{t}$ is in the direction of creeping ray travel. The bi-normal vector is given by $\hat{b} = \hat{t} \times \hat{n}$; it tracks the torsion of the geodesic. The expressions for the surface fields and surface currents created by the creeping waves will be given in terms of the local $\hat{b}$ and $\hat{t}$ unit vectors.

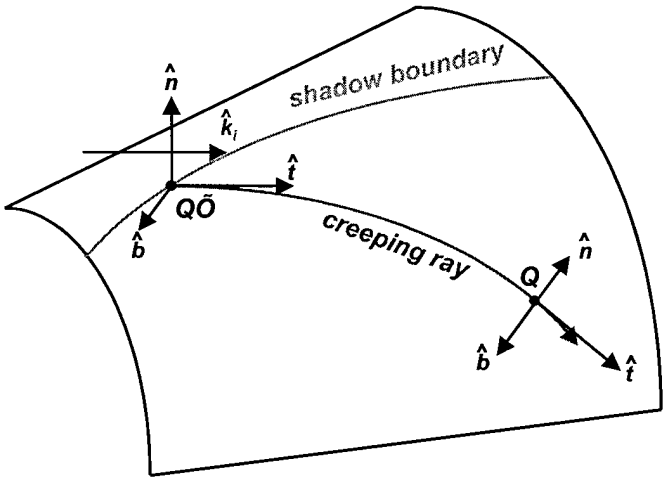

Fig. 36. Local coordinate system and notation for geodesic creeping ray arcs.

The creeping ray launches from the SB at point Q', also called the source point. Arbitrary points along the geodesic arc are labeled Q. In expressions given below, quantities like $K(Q)$ mean that function evaluated at point Q on the geodesic creeping ray arc.

Without repeating the derivation in Mitschang and Wang [13][1], the formulas for the creeping wave surface magnetic fields in the shadow region are given by

$$\overline{H}_{sh} = H_b \hat{b} + H_t \hat{t}\,, \tag{40a}$$

$$H_b = \left(\hat{n}\cdot\hat{e}^i\right)\left[F_1 - j\frac{\Lambda(Q')D^2(Q)}{k\rho_g(Q)}F_2\right] + \left(\hat{n}\cdot\hat{h}^i\right)T_0(Q')F_2\,, \tag{40b}$$

[1] Mitchang and Wang [13] assume $exp(j\omega t)$ time-harmonic dependence in their expressions, although their paper mistakenly claims $exp(-j\omega t)$ dependence at one point. This report assumes $exp(-j\omega t)$ dependence, so all phasor expressions appear as the complex conjugate of their correspondents in [13].

$$H_t = -\left(\hat{n}\cdot\hat{h}^i\right)\left[F_2 + j\frac{\Lambda(Q')D^2(Q)}{k\rho_g(Q)}F_1\right], \tag{40c}$$

where $\hat{e}^i$ and $\hat{h}^i$ are the incident plane wave polarization unit vectors for the electric and magnetic fields, respectively. Parameter Λ is the transition parameter that heuristically combines the canonical sphere and cylinder asymptotic creeping wave solutions to yield a more general solution for arbitrary convex surfaces. Λ is given by

$$\Lambda(Q') = \begin{cases} 0 & \text{, cylinder} \\ 1 & \text{, sphere} \\ R_2(Q')/R_1(Q'), & \text{general convex surfaces} \end{cases}, \tag{41}$$

where $R_1(Q')$ and $R_2(Q')$ are the principle radii of curvature at the SB launch point of the creeping ray; $R_1(Q') >= R_2(Q')$. Note that $\Lambda(Q')$ is a fixed quantity based on surface conditions at the SB, not a varying quantity along the creeping ray.

Factor $D(Q)$ in (40) is the divergence factor of the creeping ray tube. A method for obtaining $D(Q)$ at any point along the creeping ray was discussed earlier. In general, $D(Q)$ is a complex number, as discussed further in the section below on caustic crossings. $\rho_g(Q)$ is the geodesic radius of curvature at any point along the geodesic arc. It is obtained directly from (32) since $\rho_g(Q) = 1/K_{arc}(Q)$. Factor $T_0(Q')$ in (40b) is directly related to the creeping ray torsion $T(Q')$ at the SB: $T_0(Q') = T(Q')\,\rho_g(Q')$. $T(Q')$ is obtained from (34).

Factors $F_1 = F_1(Q,Q')$ and $F_2 = F_2(Q,Q')$ incorporate the Fock functions $f(\xi)$ and $g(\xi)$ governing the decay of creeping waves as they extend from the shadow boundary. F_1 and F_2 are given by

$$F_1(Q,Q') = e^{jk\tau}\left[\frac{\rho_g(Q')}{\rho_g(Q)}\right]^{1/6} D(Q)g(\xi), \tag{42a}$$

$$F_2(Q,Q') = \frac{-j}{m(Q)}e^{jk\tau}\left[\frac{\rho_g(Q')}{\rho_g(Q)}\right]^{1/6} D(Q)f(\xi). \tag{42b}$$

$\tau = \tau(Q,Q')$ is the arc length of the creeping ray measured from the SB. Expressions for the Fock functions $f(\xi)$ and $g(\xi)$ are given in (39). Fock parameter $\xi = \xi(Q,Q')$ is given by

$$\xi(Q,Q') = \int_{Q'}^{Q}\frac{m(s)}{\rho_g(s)}ds, \tag{43}$$

where

$$m(s) = m(Q) = \left(\frac{k\rho_g(Q)}{2} \right)^{1/3} . \tag{44}$$

3. Caustic Crossing

For the sphere geometry, the creeping waves reach a caustic at $\theta = \pi$. This is the point where the creeping waves launched at the SB (at $\theta = \pi/2$) converge at the pole of the sphere. Beyond the caustic, the creeping waves will again diverge until they reach the SB on the other side of the sphere from which they were launched. Beyond that point, they will again converge to a caustic, this time at $\theta = 0$. On the sphere, this process continues indefinitely as the creeping waves continue, forming successive caustics at $\theta = \pi$ and $\theta = 0$.

In the general implementation of creeping waves on doubly curved surfaces, caustics will arise. In general, they do not form points. Rather, neighboring creeping waves rays will converge over a locus of points forming a curved line on the surface. This caustic line is the 1-D correspondent to the 2-D caustic surfaces that arise in geometrical optics (GO) with the reflection of rays off of curved surfaces [15]. As in the GO case, the fields predicted by the asymptotic creeping wave solution are invalid in the immediate vicinity of the caustic, but fields both before and beyond the caustic are valid. Also, in crossing the caustic, a phase shift occurs that needs to be accounted for in the numeric implementation.

If one inspects the canonical solution of the sphere in (37), which is valid for $0 < \theta < \pi$, the expression includes extra terms for creeping waves that start at the opposite SB and travel around the back; these are the terms with subscript, 2. This is in contrast to (40), which does not implicitly account for creeping waves arriving from a different SB launch point. Doing so is not possible on general convex surfaces, and the intent with the general implementation is for this effect to be created explicitly by launching creeping wave rays from all points along the SB and allowing them to travel freely.

Returning to the sphere expressions in (37), and casting these in terms of the general solution of (40) and its $\hat{n},\hat{b},\hat{t}$ framework for specifying field and surface current directions, the phase shift for a creeping wave crossing a caustic can be deduced. Accounting for the flip in the polarization definitions of $\hat{\theta}$ and $\hat{\phi}$ at the poles, and also the relative change in orientation of the incident fields at the opposite SB point, it can be shown from (37) that the terms proportional to divergence factor D experience a -90^o (*i.e.*, $-j$) phase shift when crossing the caustic, while terms proportional to D^3 experience a $+90^o$ (*i.e.*, $+j$) phase shift.

As with the GO caustics, the creeping wave caustic phase shifts can be interpreted as arising from a generalized divergence factor D that takes on complex values. In (38a), D is real and positive because $0 < \theta < \pi$. If we recast the backside creeping wave terms in (37) that travel through the caustic to use the range, $\pi < \theta < 2\pi$, in their various arguments, then D becomes imaginary and (38a) can be re-written as,

$$D = \frac{1}{\sqrt{\sin\theta}} = \frac{-j}{\sqrt{|\sin\theta|}}, \quad \pi < \theta < 2\pi. \tag{45}$$

$\sqrt{\sin\theta}$ has branch points at $\theta = n\pi$, $n = \{...,-2,-1,0,1,...\}$.

If we choose the branch where

$$\sqrt{\sin\theta} = j^n \sqrt{\sin\theta'}, \quad \theta = \theta' + n\pi, \; 0 < \theta' < \pi,$$

then both D and D^3 take on the correct real or imaginary sign, $\{+1,+j,-1,-j\}$, in the generalized version of (37). For the generalized implementation of Eqs. (40) – (44), whenever a caustic is encountered in evaluating D in (31), a $-j$ factor should be applied to D while traveling forward through the caustic. For the D^3 terms, this factor should be included before cubing D.

4. Uniform Solution For Lit Region

Equation (40) describes the creeping wave surface currents in the shadow region. If these are combined with the PO surface currents in the lit region, there will be an abrupt discontinuity at the SB. This is because PO breaks down near the SB. Since one of the important goals of the creeping wave formulation is to improve over PO near the SB, not just in the deep shadow region, researchers have developed generalized expressions based on the Fock's asymptotic solution that can be used in the lit region and create a smooth transition over the SB. For the lit region coordinate system shown in Fig. 37, Mitschang and Wang [13] give the following expression for fields in the lit region:

$$\overline{H}_{lit} = \left(\hat{e}^i \cdot \hat{n}'\right) F_1^{lit} \hat{b} - \left(\hat{h}^i \cdot \hat{n}'\right) F_2^{lit} \hat{t}, \tag{46}$$

where

$$F_1^{lit} = e^{jk\tau_l} g\left(\xi_l\right), \tag{47a}$$

$$F_2^{lit} = \frac{-j}{m_l(Q)} e^{jk\tau_l} f\left(\xi_l\right), \tag{47b}$$

and

$$\xi_l(Q) = -m_l(Q)\cos\theta_i, \tag{48a}$$

$$m_l(Q) = \frac{m(Q)}{\left[1 + T_0^2(Q)\cos^2\theta_i\right]^{1/3}}, \tag{48b}$$

$$\tau_l = \hat{k}^i \cdot \overline{r} + \frac{\xi_l^3}{3k}. \tag{48c}$$

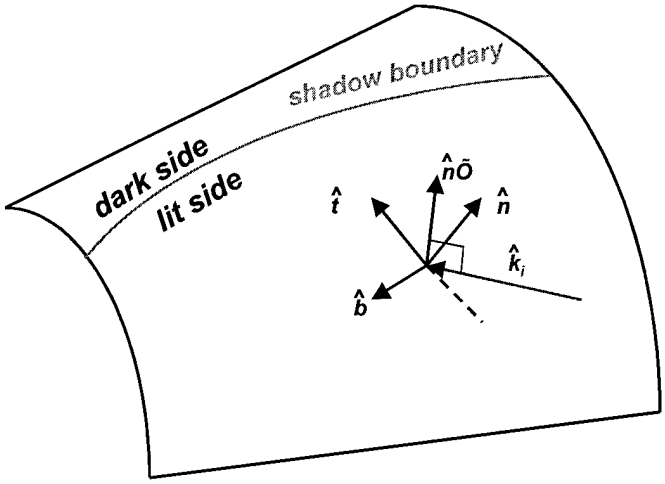

Fig. 37. Coordinate system for lit region.

Note that in Equation (48b), the torsion-related parameter is evaluated at the point of incidence Q rather at the shadow boundary Q'. This is because we are in the lit region and all points are "source" points. Also, the quantity $m(Q)$ in (48b) is evaluated using (44) based on the curvature along the tangent direction defined in Fig. 37.

It should be pointed out that the expression in (46) lacks the second-order $(1/k)$ terms present in (40) arising from the sphere solution in (37). Hence, there will still be a small discontinuity in the surface currents. This effect is evident in the numerical results we present later for the sphere using the generalized formulation. Also, Pathak [12] gives an expression that they claim maintains continuity at the SB, and which includes additional terms relating to the surface torsion beyond those given in (46). At the time of this reporting, we are conducting further investigation into this issue to resolve these discrepancies and obtain a uniform solution across the SB.

E. Results and Discussion

To test the reasonableness of the formulation for the shadow region creeping wave surface currents, the study code was employed to predict results on a sphere and cylinder with hemisphere end caps. The surface currents are shown on the target bodies in Figs. 38 and 39.

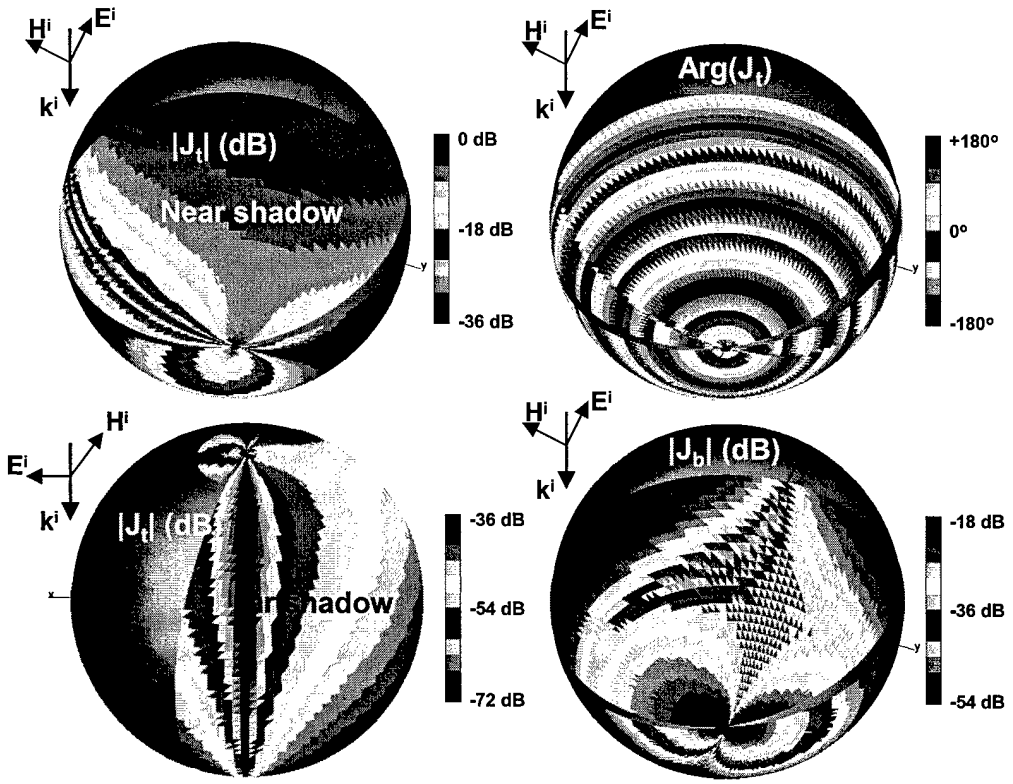

Fig. 38. Predicted shadow region creeping wave currents on a sphere. Only a subset of the creeping waves are shown launching from a roughly *170°* portion of the incident shadow boundary in order to clearly illustrate currents in both the near and far shadow regions.

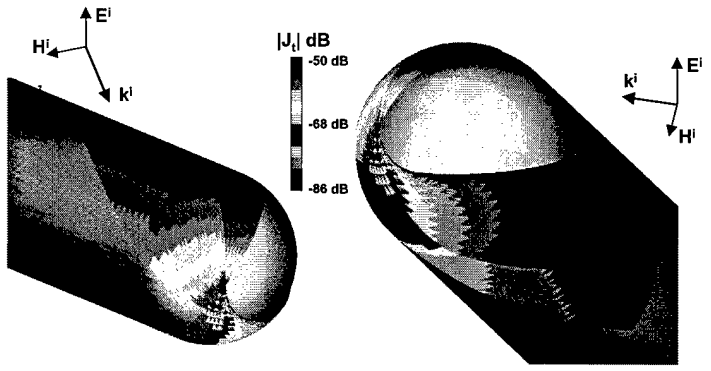

Fig. 39. Predicted shadow region creeping wave currents on a cylinder with hemisphere caps. For clarity, only a subset section of the creeping wave are shown.

Inspecting the surface currents, several things are evident. First, the magnitudes of the currents generally decrease as they travel, corresponding to their progressive radiation to space. Mathematically, this arises directly from the large positive argument behavior of the Fock functions. Also, as the surface currents approach a caustic, their intensity increases toward a singularity; this is most evident for the sphere geometry in Fig. 38. The singularity arises directly from the divergence factor. Surface currents immediately near the caustics are not shown (*i.e.*,

painted black) in Figs. 38 and 39. This corresponds directly to the logic in the study code for skipping the surface integration near the caustic to avoid a divergent result. In the case of the sphere in Fig. 38, the geodesics converge on a point caustic. That is a special case. For the more general shape in Fig. 39, the loci of the caustics are curved lines. Finally, the representation of surface current phase reveals the expected steady progression arising directly from the exponential factors in (42).

To further verify the numeric implementation of the general formulation, scattering computations were performed on the sphere geometry (radius $a = 2\ m$) and compared to both the exact Mie series solution and physical optics. The time response (*i.e.*, range profile) is given in Fig. 40 and the frequency response in Fig. 41

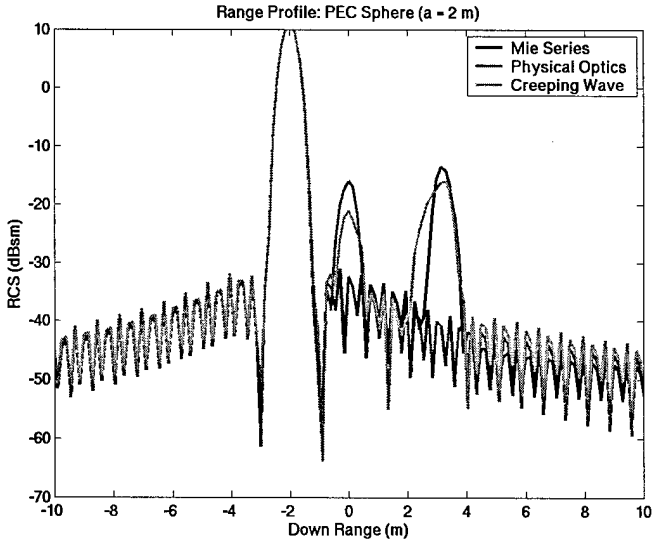

Fig. 40. Back-scattering time response (range profile) for a PEC sphere (radius $a = 2\ m$) computed from exact solution (Mie) series, physical optics, and numeric implementation of the generalized creeping wave ray tracer.

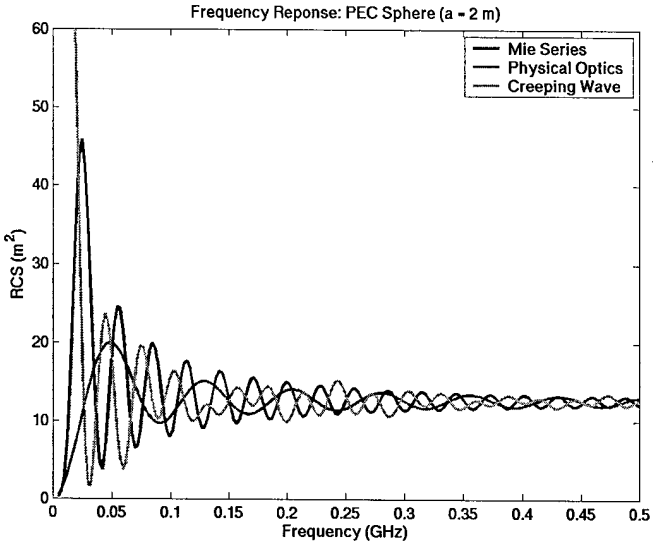

Fig. 41. Back-scattering frequency response for a PEC sphere (radius $a = 2\ m$) by exact solution, physical optics, and generalized creeping wave ray tracer.

For the range profile in Fig. 40, we observe that the generalized implementation reintroduces the false scattering feature at $z = 0$, as compared with the more accurate results based on the specialized formulation for the sphere (37) in Fig. 35. This is caused by the remaining discontinuity in surface currents around the SB arising from inconsistencies between the shadow region formation of (40) and the lit region formulation of (46). This was discussed earlier, and our current work centers on reconciling these two representations. Also, the numeric implementation of (46) in the study code has not been firmly established by our own inspection of the source code at this reporting. Nonetheless, even in the current implementation, this spurious feature is reduced relative to PO.

Because of the limited bandwidth in the computed frequency response, in the range profile from the general creeping wave implementation, the false scattering feature at $z = a(\pi/2 + 1)/2 = 2.57\ m$ is not completely resolved from the trailing response at $z = a\pi/2 = 3.14\ m$ due to emergence creeping wave back into the lit region. However, its effect is observed in the widened and distorted response feature in the vicinity of these two locations. This spurious feature was also evident in the higher-resolution range profile based on the specialized formulation of the sphere in Fig. 35. As discussed earlier, this is caused by abruptly halting the surface integration in the vicinity of the caustic at the pole. This situation should be improved by instead smoothing the surface currents around the caustic to avoid a non-integrable singularity (caused by breakdown of the creeping wave formulation), but this remains to be tested numerically. Finally, the trailing response due to the emergence of the creeping waves back into the lit side after traveling around the back is properly produced by the generalized implementation of the asymptotic creeping wave formulation.

Correspondingly, the frequency response in Fig. 41 also suffers in the generalized implementation. This is caused by the same effects just discussed. In spite of these remaining problems, it still represents an improvement over the PO solution in terms of picking up the higher rate of oscillation about the final RCS level converged upon for $k_0 a >> 1$. If the

remaining issues of the SB discontinuity can be resolved, the generalized creeping wave implementation holds strong promise for greatly improving upon the base PO solution of Xpatch®.

F. Summary

A complete method was presented for improving the performance of Xpatch® in the deep shadow region on smoothly curved bodies using a creeping wave approach that is consistent with the Xpatch® framework of approximating surface currents on arbitrary target geometries through ray tracing. This included an alternate technique for identifying the shadow boundary on the target, which was qualitatively compared with the original SB-finding technique developed in this project for implementation of the SB-ILDCs. The overall method also included numeric approaches for tracing the geodesic creeping wave rays from the shadow boundary and developing appropriate surface currents along them from asymptotic formulations based on the Fock theory.

These methods were implemented in a research code employed by this study and tested on simple cases. Based on this evaluation, we reach the following conclusions. First, the alternate method for finding the SB appears workable, and is well-suited toward the application of launching creeping waves in the shadow region since it constructs the SB as a contiguous curve that can be re-sampled. However, further work is required in adapting it to more complex geometries that contain multiple SBs. Second, the method for tracing the geodesic creeping wave rays behaved both reasonably and efficiently on the curved surface geometries considered. This included the ability to carry the geodesics across adjoining patches whose topological links were not established *a priori* as input to the code, an important practical benefit to the method described. Third, and finally, the method for applying shadow region surface currents to the creeping wave rays improved the scattering solution on the sphere test case considered. However, discontinuities in the lit side and shadow side formulations remain that still cause undesirable scattering features in the generalized implementation. Our current work focuses on examining this issue further so that these non-physical SB discontinuities in the surface currents can be eliminated.

VI. CONCLUSIONS

The Xpatch® code with the SB-ILDCs shows a large improvement in calculating the scattering from a number of objects. Large cylinders and spheres were modeled. The effectiveness of the SB-ILDCs was illustrated for objects with different sized radii of curvature and for objects that possess a varying radii of curvature.

The Xpatch® code with the TW-ILDCs calculates with greater accuracy the scattering from objects with edges. The new TW-ILDCs eliminate the integration singularities present in the old formulation and produce scattering results that are free of the previous non-physical field discontinuities. The original Xpatch® formulation lacked cross-polarization terms (infinity avoidance). The TW-ILDCs are based on a rigorous derivation that includes cross terms. The TW-ILDCs also achieve a partial accounting of 2nd order diffraction effects.

A detailed study of deep shadow creeping wave scattering as a means of supplementing the SB-ILDC work was performed. This study employed a prototype algorithm for tracing creeping waves along smoothly curved bodies. This algorithm consists of a geometrical component in which contiguous shadow boundary contours are extracted followed by geodesic ray tracing component to determine the paths of creeping waves launched at the shadow boundary. Details of the underlying creeping wave EM radiation formulation were presented along with numerical results for the sphere and hemisphere-capped circular cylinder. Comparisons with closed form and full wave results are good and demonstrate the added physics due to the late time scattering of creeping waves. However, the underlying EM approach possesses significant shortcomings with respect to caustic points along the geodesic path. Future research will explore development within an ILDC framework in which direct calculation of the surface currents can be avoided in favor of more stable line integral representations of the scattering.

VII REFERENCES

[1] R. A. Shore and A. D. Yaghjian, "Shadow Boundary Incremental Length Diffraction Coefficients Applied to Scattering from 3-D Bodies," *IEEE Trans. Antennas and Propagat.*, v. AP-49, No. 2, Feb. 2001.

[2] J. J. Bowman, T. B. A. Senior, and P. L. E. Uslenghi, Sections 2.2.1.3 and 2.2.2.3, *Electromagnetic and Acoustic Scattering by Simple Shapes*, North Holland Publishing Company, Amsterdam, 1969.

[3] A. D. Yaghjian, R. A. Shore, and M. B. Woodworth, "Shadow boundary incremental length diffraction coefficients for perfectly conducting smooth, convex surfaces," *Radio Sci.*, vol. 31, no. 6, pp. 1681-1695, Nov/Dec 1996.

[4] P.Y. Ufimtsev, "Method of edge waves in the physical theory of diffraction," *Electromagn.*, vol. 11, no. 2, pp. 125-160. Apr/Jun 1991.

[5] K.M. Mitzner, "Incremental length diffraction coefficients," *Tech. Rep. AFAL-TR-73-296.*, Northrop Corp. Apr 1974.

[6] A. Michaeli, "Equivalent edge currents for arbitrary aspects of observation," *IEEE Trans. Antennas Propagat.*, vol. 32, pp. 252-258, Mar. 1984.

[7] R.A. Shore and A.D. Yaghjian, "Incremental diffraction coefficients for planar surfaces," *IEEE Trans. Antennas Propagat.*, vol. 36, pp. 55-70, Jan 1988.

[8] P.M. Johansen, "Uniform physical theory of diffraction equivalent edge currents for truncated wedge strips", *IEEE Trans. Antennas Propagat.*, vol. 44, no. 7, Jul 1996.

[9] L.P. Ivrissimtzis and R.J. Marhefka, "A uniform ray approximation of the scattering by polyhedral structures including higher order terms," *IEEE Trans. Antennas Propagat.*, vol. 40, no. 11, Nov 1992.

[10] S. W. Lee, *Geometrical Theory of Diffraction*, Vol. II, *"Differential Geometry for GTD Applications,"* EM Publishing Co., Champaign, IL, 1983

[11] D. J. Struik, *Differential Geometry*, 2nd Edition, Addison-Wesley, Reading, MA, 1961.

[12] P. H. Pathak, N. Wang, W. D. Burnside, and R. G. Kouyoumjian, "A uniform GTD solution for the radiation from sources on convex surfaces," *IEEE Trans. Antennas Propagat.*, Vol. AP-29, No. 4, July 1981, pp. 609 – 622.

[13] L. N. Medgyesi-Mitschang and D-S Wang, "Hybrid solutions for scattering from perfectly conducting bodies of revolution," *IEEE Trans. Antennas Propagat.*, Vol. AP-31, No. 4, July 1983, pp. 570 – 583.

[14] G. T. Ruck, Ed., *Radar Cross Section Handbook*, Vol. 1, Plenum Press, New York, 1970.

[15] S. W. Lee, *Geometrical Theory of Diffraction*, Vol. III, *"Geometrical Optics,"* EM Publishing Co., Champaign, IL, 1983.